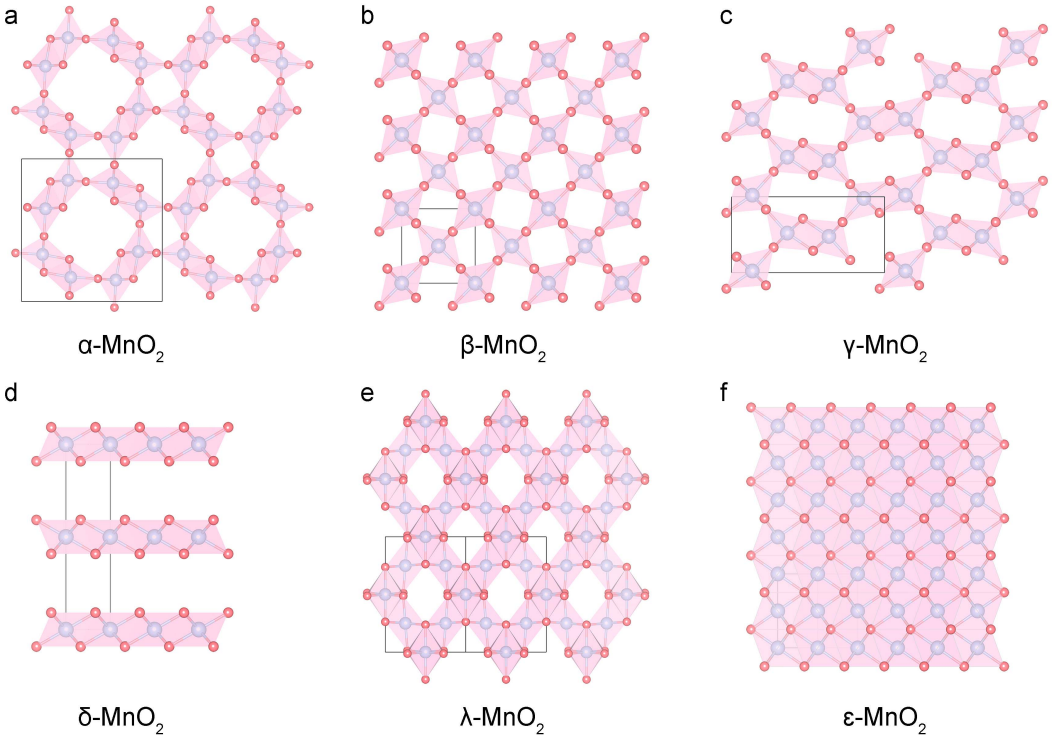
Supplementary Information

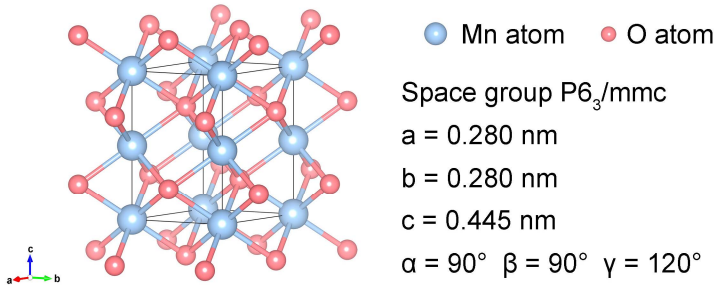
Lattice-oxygen topology engineering to enable durable and high-efficiency aqueous manganese batteries

Zefang Yang,[1 2] Yuhang Liu,[1] Jinchi Li,[1] Lin Liu,[1] Yifeng Wang,[1] Fulong Zhu,[1] Hongrun Jin,[1] Wanhai Zhou,[1] Yonggang Wang,[3] Hong Jin Fan,[2] Dongyuan Zhao,[1] Dongliang Chao*[1]

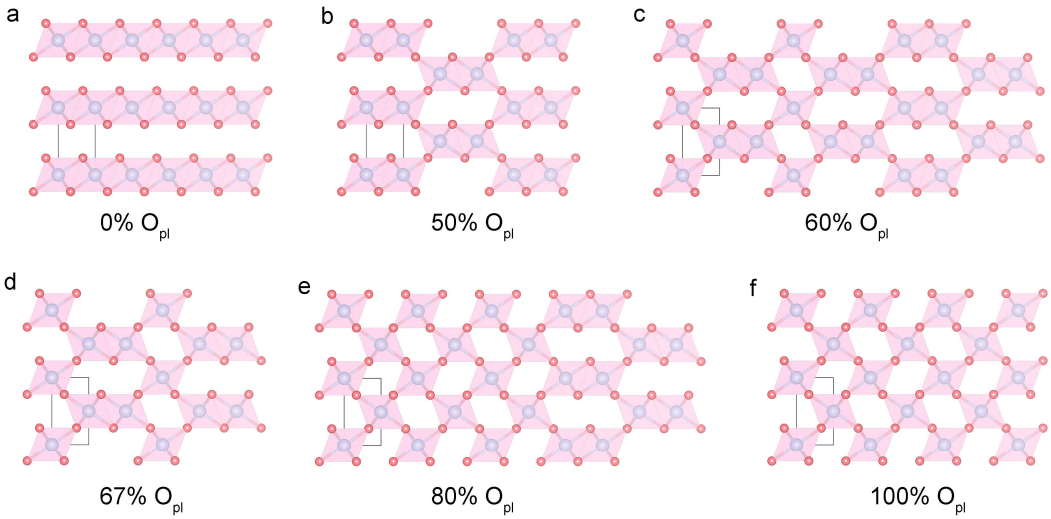
[1]Laboratory of Advanced Materials, Aqueous Battery Center, State Key Laboratory of Molecular Engineering of Polymers, College of Smart Materials and Future Energy, Fudan University, Shanghai, 200433, P. R. China
E-mail: chaod@fudan.edu.cn
[2]School of Physical and Mathematical Sciences, Nanyang Technological University, Singapore 637371, Singapore
E-mail: fanhj@ntu.edu.sg
[3]Department of Chemistry and Shanghai Key Laboratory of Molecular Catalysis and Innovative Materials, Institute of New Energy, iChEM (Collaborative Innovation Center of Chemistry for Energy Materials), Fudan University, Shanghai 200433, P. R. China



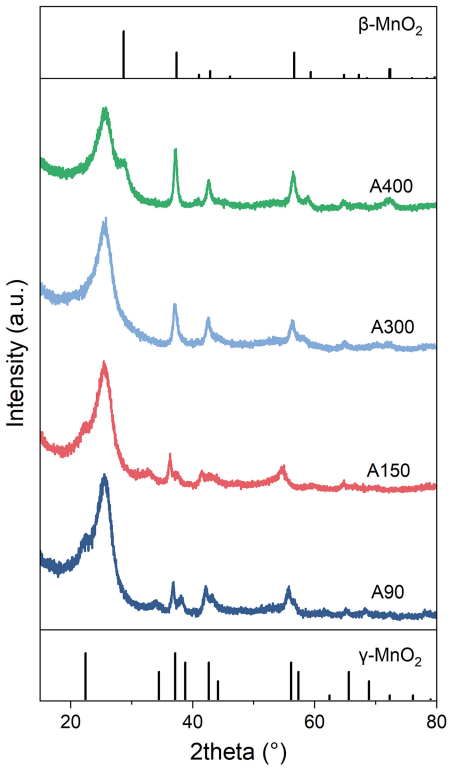
Supplementary Fig. 1 MnO_2 polymorph frameworks with Mn-O_6 octahedral connectivity motifs. Atomic structure models of (a) α-, (b) β-, (c) γ-, (d) δ-, (e) λ-, and (f) ε-MnO_2. The blue and red balls refer to Mn and O atoms, respectively. The boxes represent lattice of a unit cell.



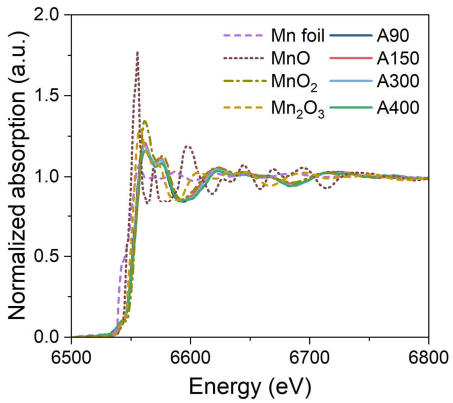
Supplementary Fig. 2 The ideal ε-MnO_2 crystalline structure. The ε-MnO_2 unit cell and its lattice parameters.



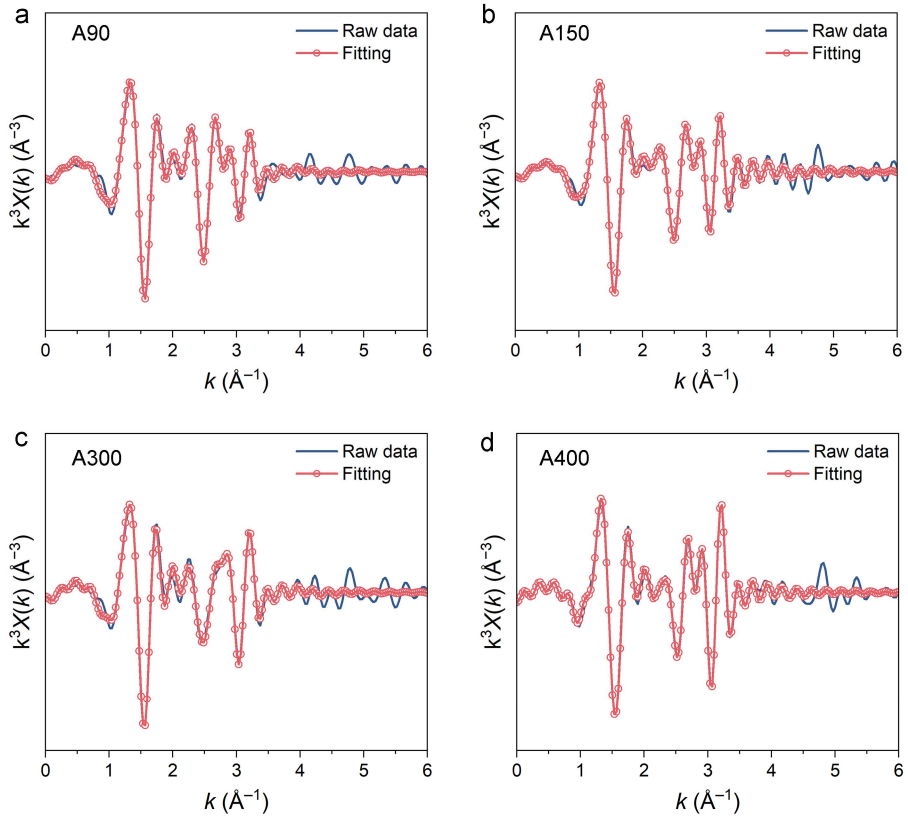
Supplementary Fig. 3 The possible ε-MnO_2 structure models with different Opl fractions. The atomic structure of ε-MnO_2 with the O_{pl} fractions of (a) 0%, (b) 50%, (c) 60%, (d) 67%, (e) 80%, and 100%. In all these models, Mn^{4+} cations occupy 50% of the Mn-O octahedral sites. The boxes represent lattice of the original ε-MnO_2 structures.



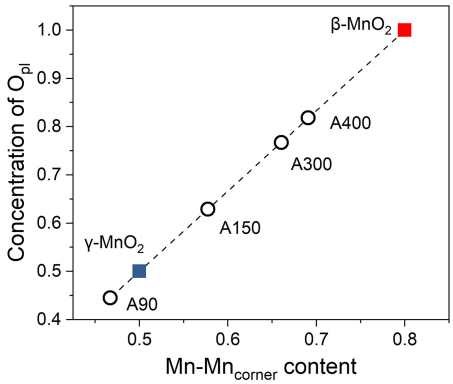
Supplementary Fig. 4 XRD analysis of the prepared MnO_2 samples. XRD patterns of A90, A150, A300, and A400, indexed between γ-MnO_2 (JCPDS 14-0644) and β-MnO_2 (JCPDS 24-0735) reference reflections.



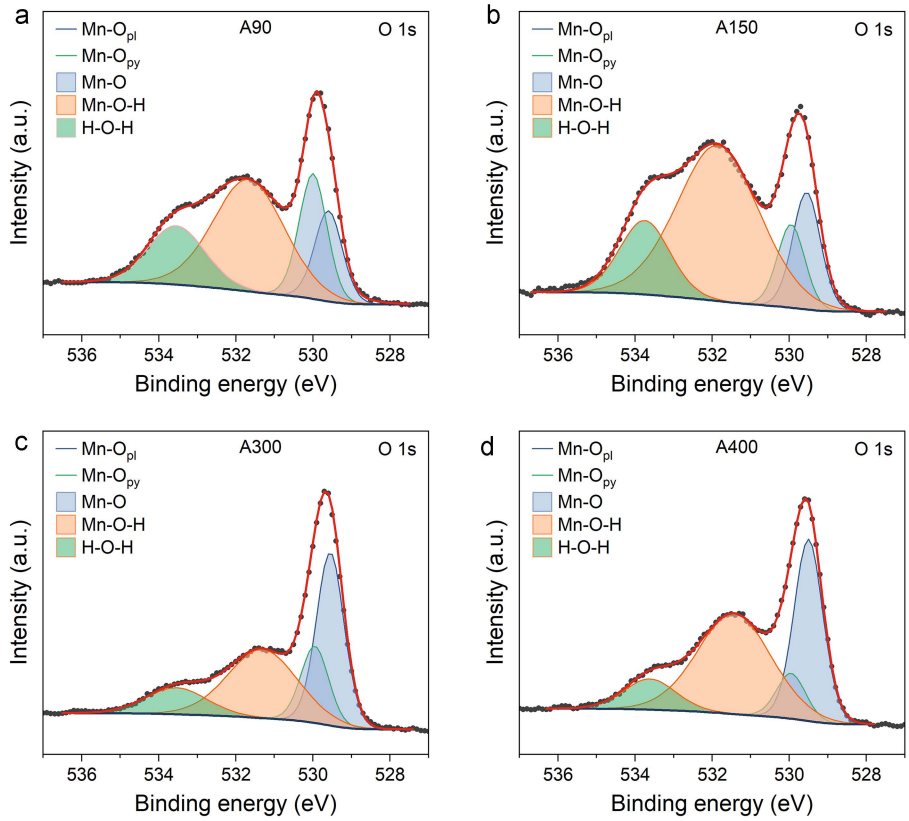
Supplementary Fig. 5 Mn K-edge XANES spectra of the prepared MnO_2 samples. Normalized Mn K-edge XANES spectra of A90, A150, A300, and A400, compared with Mn foil, MnO, Mn_2O_3, and MnO_2 references.



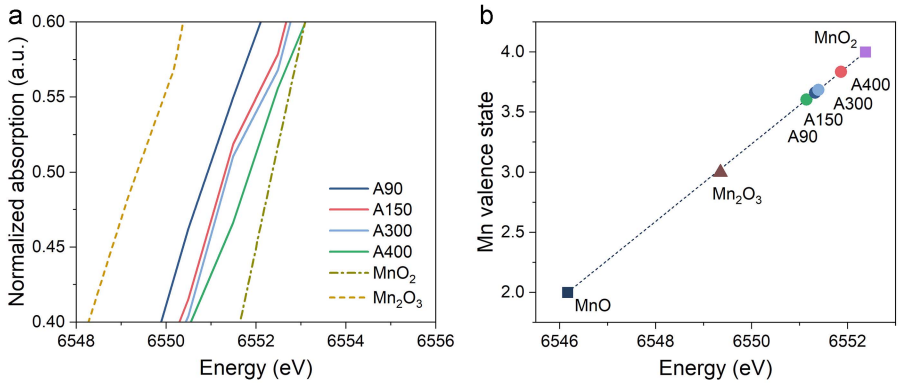
Supplementary Fig. 6 EXAFS k-space fitting of the prepared MnO_2 samples. k^3-weighted χ(k) spectra and corresponding fitting results of of (a) A90, (b) A150, (c) A300, and (d) A400. The Mn-Mn_{corner} contents were calculated by $A_c \times r_c/(A_c \times r_c + A_e \times r_e)$, where A_c and A_e were the integrated area of Mn-Mn_{corner} and Mn-Mn_{edge} peak in EXAFS, respectively, r_c and r_e were the peak position of Mn-Mn_{corner} and Mn-Mn_{edge}, respectively. The fitted parameters are shown in Supplementary Table 1.



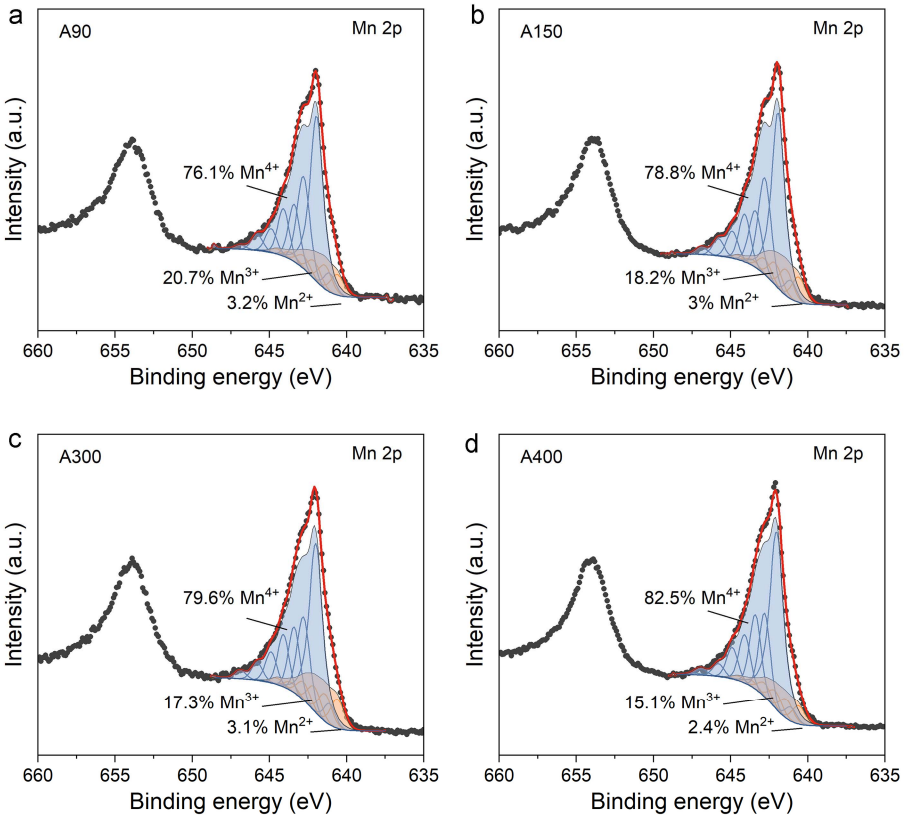
Supplementary Fig. 7 Quantitative analysis O_{pl} fractions in EXAFS. The calculated O_{pl} concentration of A90, A150, A300, and A400 based on the EXAFS results with the reference of γ-MnO_2 and β-MnO_2.



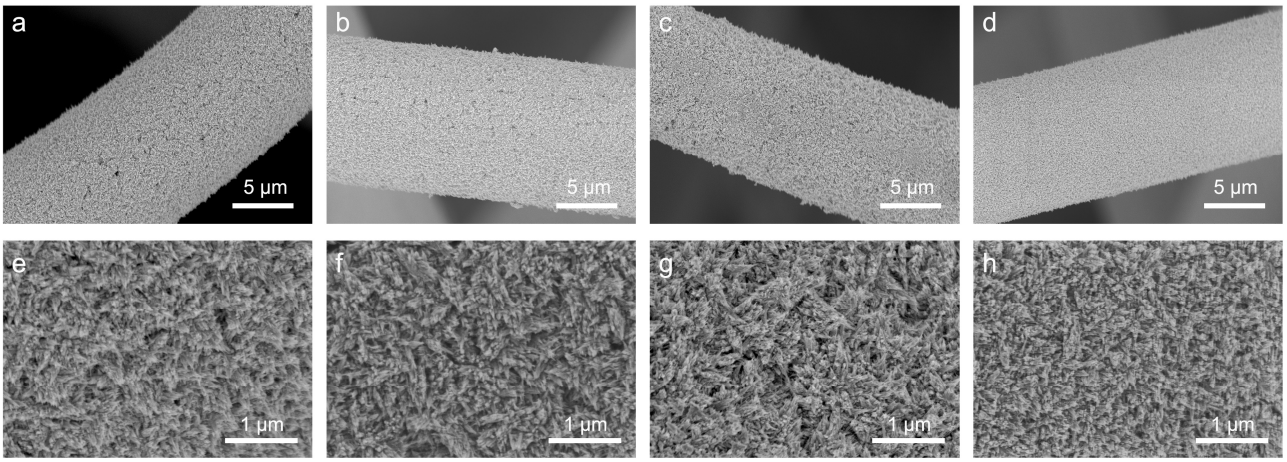
Supplementary Fig. 8 O 1s spectra the prepared MnO_2 samples. XPS spectra of O 1s in (a) A90, (b) A150, (c) A300, and (d) A400. The peaks in the O 1s spectra are deconvoluted into Mn-O (529.7 eV), Mn-O-H (531.5 eV) and H-O-H (533.4) bond[1]. The O_{pl} concentration was calculated by fitting the XPS data with 529.9 eV for O_{py} and 539.5 eV for O_{pl}. The fitting parameters and results are provided in Supplementary Table 2.



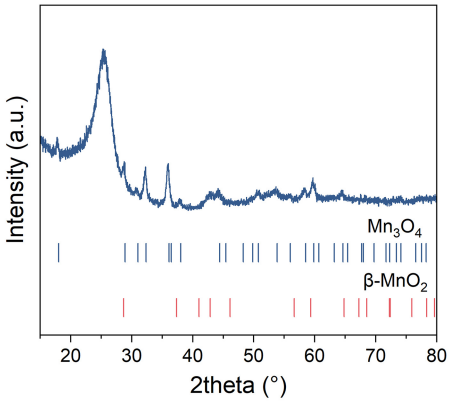
Supplementary Fig. 9 Mn K-edge XANES analysis of the prepared MnO_2 samples. (a) The enlarged Mn K-edge XANES spectra of A90, A150, A300, and A400. (b) Linear relationship plots between Mn oxidation state and edge energy (defined with a normalized adsorption height of 0.5). MnO, MnO_2, and Mn_2O_3 serve as reference samples.



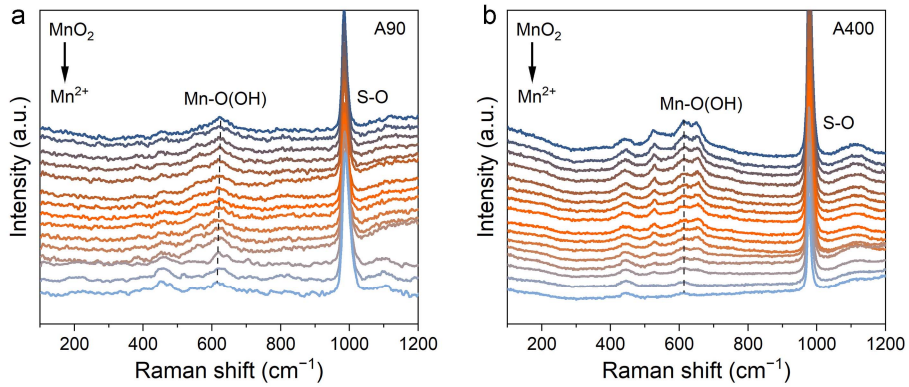
Supplementary Fig. 10 Mn 2p spectra the prepared MnO_2 samples. XPS spectra Mn 2p in (a) A90, (b) A150, (c) A300, and (d) A400. The Mn oxidation states were fitted with specified Mn^{4+}, Mn^{3+}, and Mn^{2+} species and full width at half maximum. The XPS spectra were calibrated via the normal C peak at 284.8 eV before the fitting. Fitting parameters and results are provided in Supplementary Table 3.



Supplementary Fig. 11 The morphology of the prepared MnO2 samples. SEM images of (a, e) A90, (b, f) A150, (c, g) A300 and (d, h) A400.

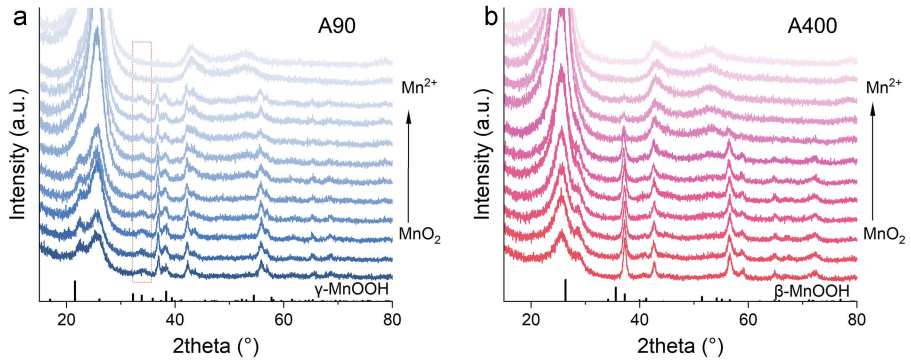


Supplementary Fig. 12 XRD analysis of the Mn_3O_4. XRD patterns of A90 after annealing at 450 °C. It can be seen from XRD patterns of A90 after annealing at 450 °C that Mn_3O_4 as the primary component with small amounts of β-MnO_2.

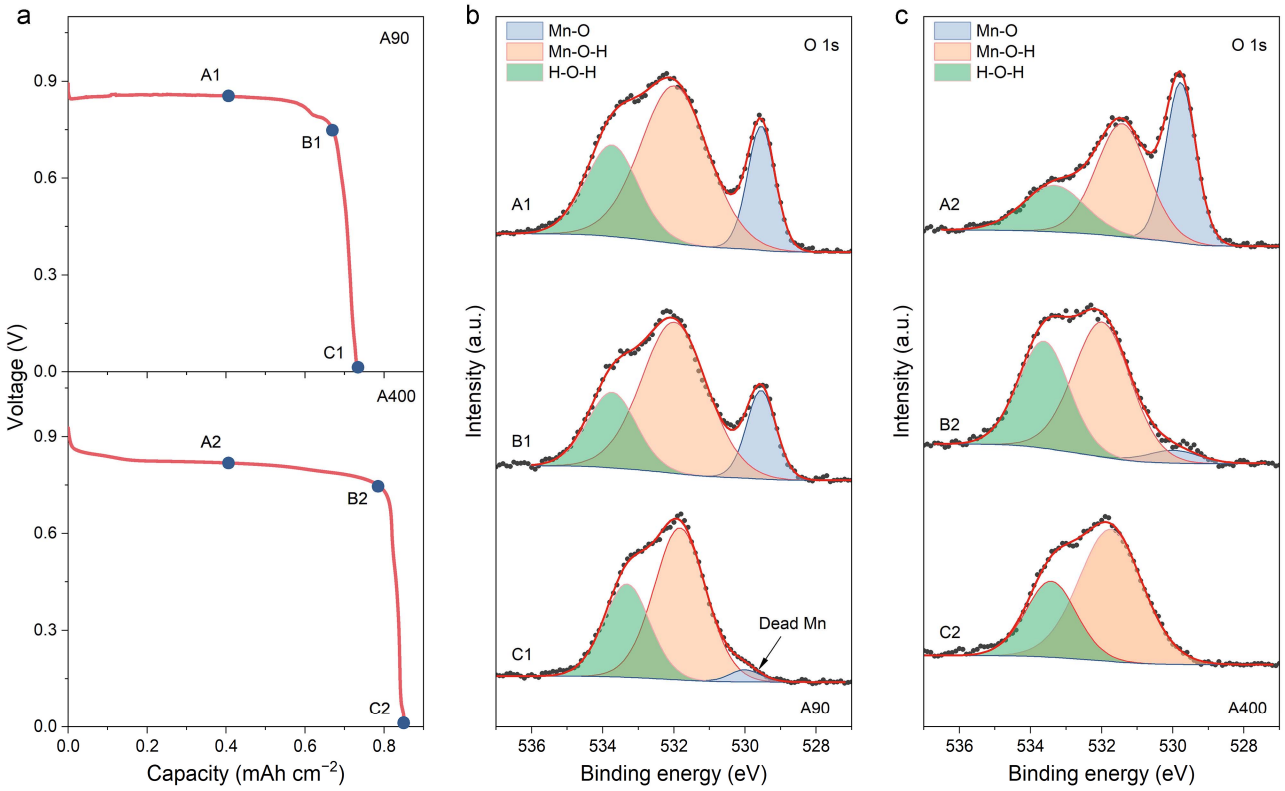


Supplementary Fig. 13 In situ Raman analysis of the prepared MnO_2 samples during dissolution. In situ Raman spectra of (a) A90 and (b) A400 during discharge with a conversion from MnO_2 to Mn^{2+}. The observed peaks at 623 and 987 cm^{-1} are assigned to the Mn-O stretching vibration of MnO_2 and

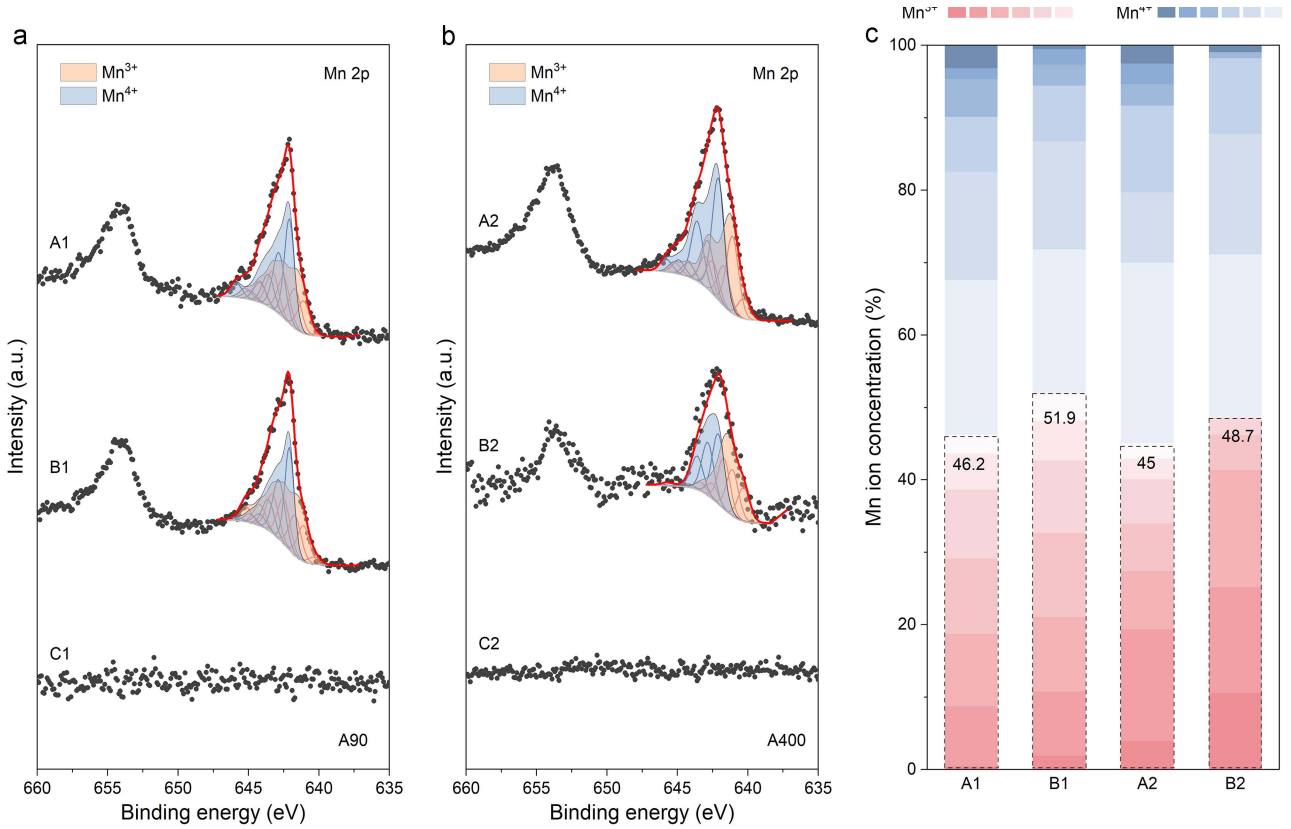
the S-O stretching vibration of the SO_4^{2-} radical in the electrolyte, respectively[2,3]. The intensity of the Mn-O bond gradually diminishes and undergoes a red shift in both A90 and A400 as discharge progresses. The red shift in A90 is 9.9 cm^{-1} greater than that in A400 (1.2 cm^{-1}), indicating the formation of MnOOH intermediates during MnO_2 dissolution, as evidenced by the characteristic peak at 614.8 cm^{-1} corresponding to Mn-O vibrations in MnOOH[4].



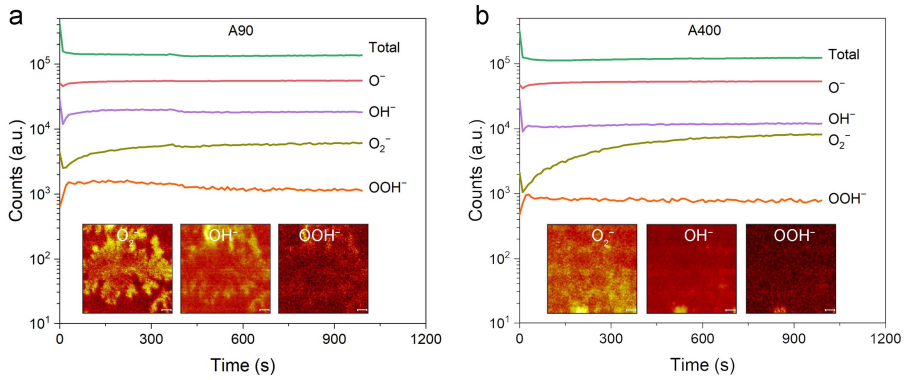
Supplementary Fig. 14 In situ XRD analysis of the prepared MnO_2 samples during dissolution. In situ XRD patterns of (a) A90 and (b) A400 during discharge with a conversion from MnO_2 to Mn^{2+}. The peak at 33.8 ° in the XRD pattern of A90 exhibits an enhanced intensity during discharge, whereas all other peaks gradually diminish as MnO_2 dissolves. This peak is indexed as γ-MnOOH (JCPDS 89-2354), suggesting the formation of MnOOH intermediates during the dissolution of A90. However, no characteristic peaks associated with β-MnOOH (JCPDS 74-1842) are observed in the XRD pattern of A400 during discharge.



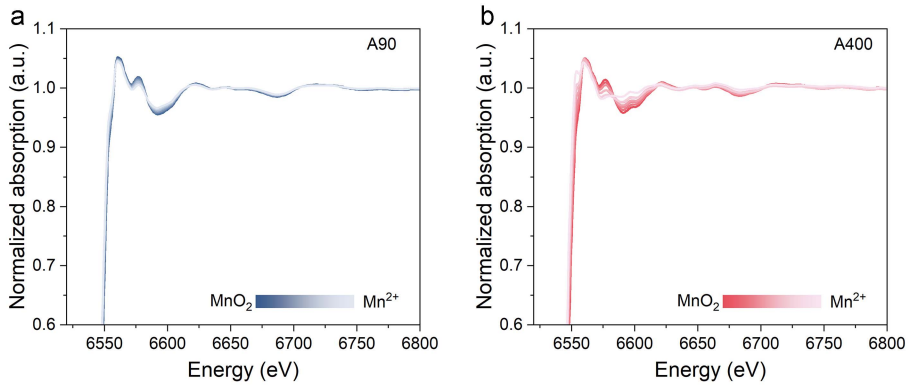
Supplementary Fig. 15 O 1s spectra of the prepared MnO_2 at different states of discharge. (a) Voltage curves of A90 and A400 during discharge. The marked A_i (discharge for 0.4 mAh cm^{-2}) B_i (discharge to 0.75 V) and C_i (discharge to 0 V) (i=1, 2) represent different states of discharge for XPS measurements. XPS spectra of O 1s in (b) A90 and (c) A400 at different states of discharge. The intensity of the Mn-O bond in A400 is gradually weakened and disappeared during MnO_2 dissolution, indicating complete dissolution of MnO_2 upon discharge to 0 V. However, a Mn-O peak is detected in A90 after discharge to 0 V, which is attributed to dead Mn induced by Mn^{3+} disproportionation from the formed MnOOH intermediate.



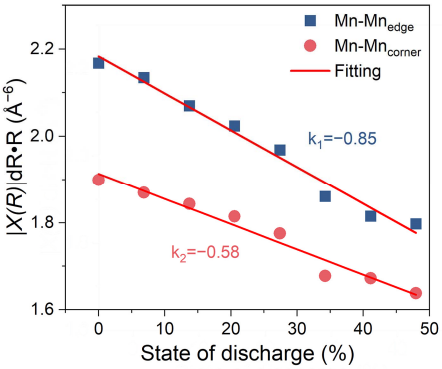
Supplementary Fig. 16 Mn valence state analysis of the prepared MnO_2 at different states of discharge. XPS spectra of Mn 2p in (b) A90 and (c) A400 at different states of discharge (marked by Supplementary Fig. 15a). (c) Mn ions concentration at different states of discharge. The Mn oxidation states were fitted with specified Mn^{4+} and Mn^{3+} species and full width at half maximum[5]. The XPS spectra were calibrated via the normal C peak at 284.8 eV before the fitting. Fitting parameters and results are provided in Supplementary Table 4.



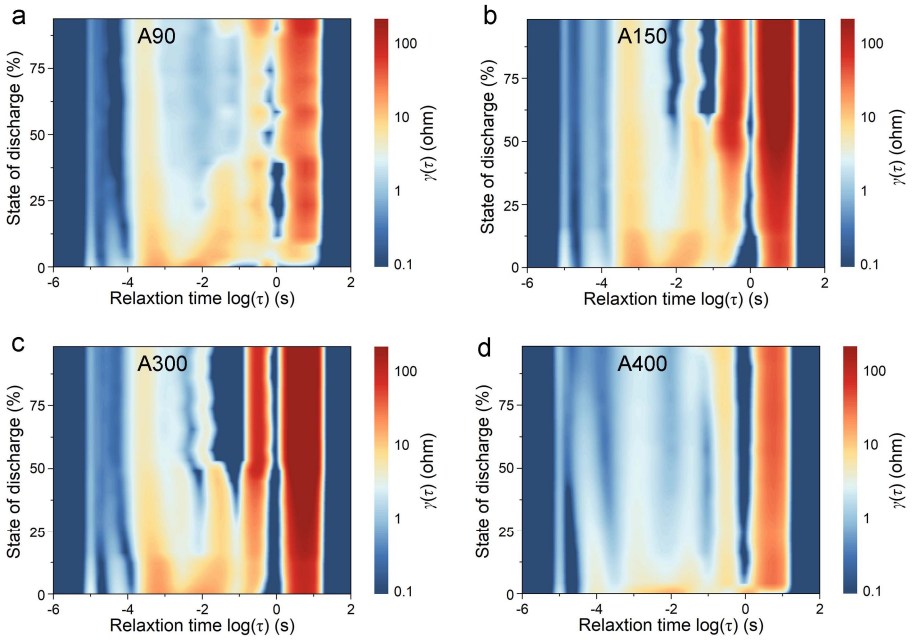
Supplementary Fig. 17 Ion distribution of A90 and A400 upon discharge. TOF-SIMS profiles and corresponding mapping results of (a) A90 and (b) A400 after discharge to 0.75 V. Ion fragments of A90 and A400 were collected via TOF-SIMS measurement in anion mode. The intensity of the O^- fragment in A400 gradually increases with sputtering time and is higher than that in A90. The OH^- and OOH^- contents in A90 are higher than those in A400, corroborating that MnO_2 is the primary component in A400, whereas A90 is dominated by MnOOH.



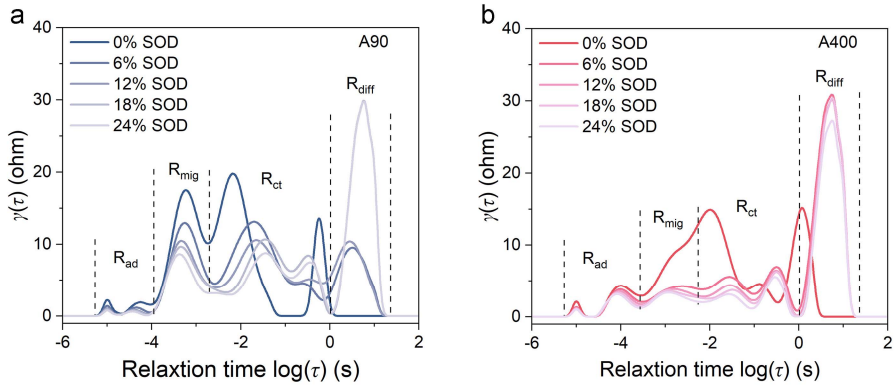
Supplementary Fig. 18 In situ synchrotron XAFS analysis of MnO_2 dissolution. Normalized in situ Mn K-edge XANES spectra of (a) A90 and (b) A400 during discharge.



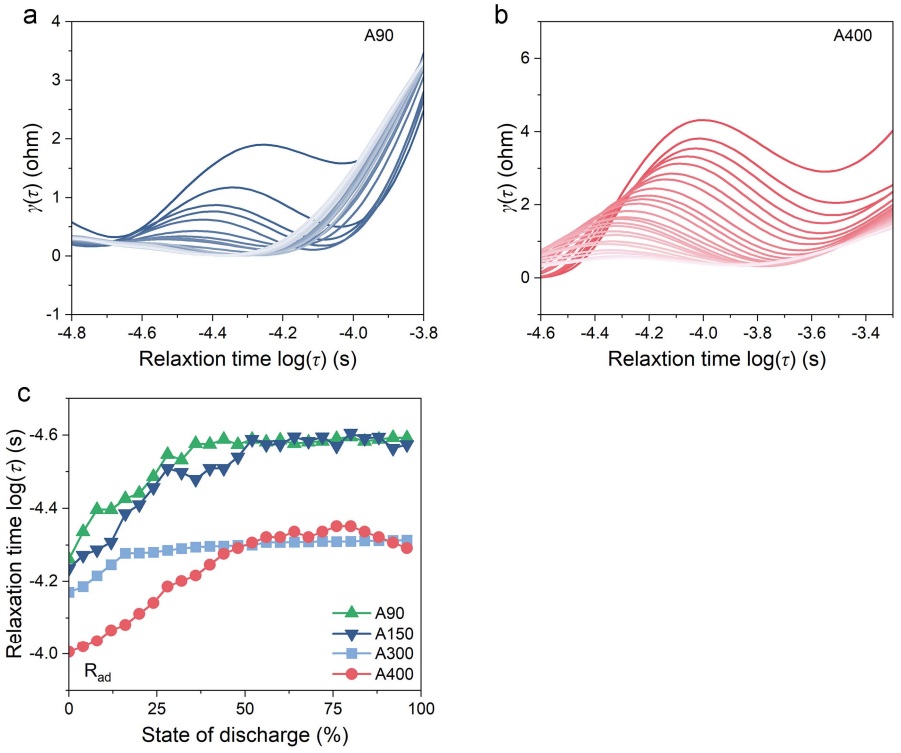
Supplementary Fig. 19 Mn-Mn pair dissolution analysis by in situ XAFS. Mn-Mn_{edge} and Mn-Mn_{corner} fraction of A90 during discharge at different states. The Mn-Mn_{edge} contents were calculated by $A_e \times r_e/(A_c \times r_c + A_e \times r_e)$, where A_c and A_e were the integrated area of Mn-Mn_{corner} and Mn-Mn_{edge} peak in Mn K-edge EXAFS of A90, respectively, r_c and r_e were the peak position of Mn-Mn_{corner} and Mn-Mn_{edge}, respectively. Through linear fitting of the Mn-Mn pair fraction at different states of discharge, the slopes for Mn-Mn_{edge} and Mn-Mn_{corner} are determined to be −0.85 and −0.58, respectively, suggesting that dissolution through the Mn-Mn_{edge} pathway is superior to that via the Mn-Mn_{corner} pathway.



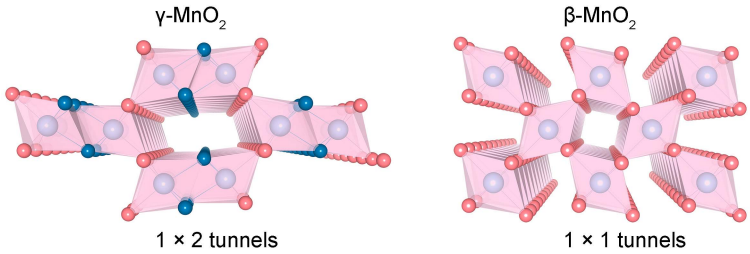
Supplementary Fig. 20 The DRT results of the prepared MnO_2 samples. DRT mapping of (a) A90, (b) A150, (c) A300 and (d) A400 during discharge.



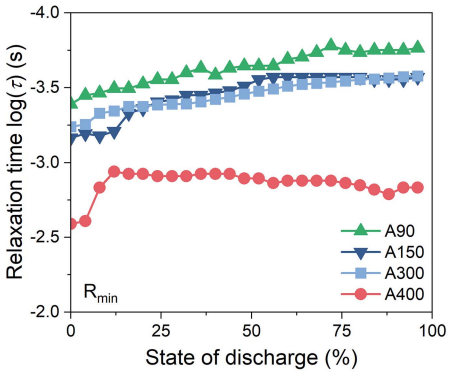
Supplementary Fig. 21 The DRT analysis of MnO_2 upon discharge. DRT curves of (a) A90 and (b) A400 at different states of discharge (SOD). The electrolytic dissolution of MnO_2 involves proton adsorption, water molecule dissociation, and Mn^{2+} dissolution migration. The τ values ranging from 5.37×10^{-6} to 4.46×10^{-4} s can be assigned to the contact resistance of proton adsorption (R_{ad}). Mn ion migration (R_{mig}) and charge transfer resistances (R_{ct}) correspond to τ values of 4.46×10^{-4} to 5.37×10^{-3} s and 5.37×10^{-3} to 1 s, respectively. The peak located from 1 to 22.9 s is attributed to mass transport (R_{diff})[6].



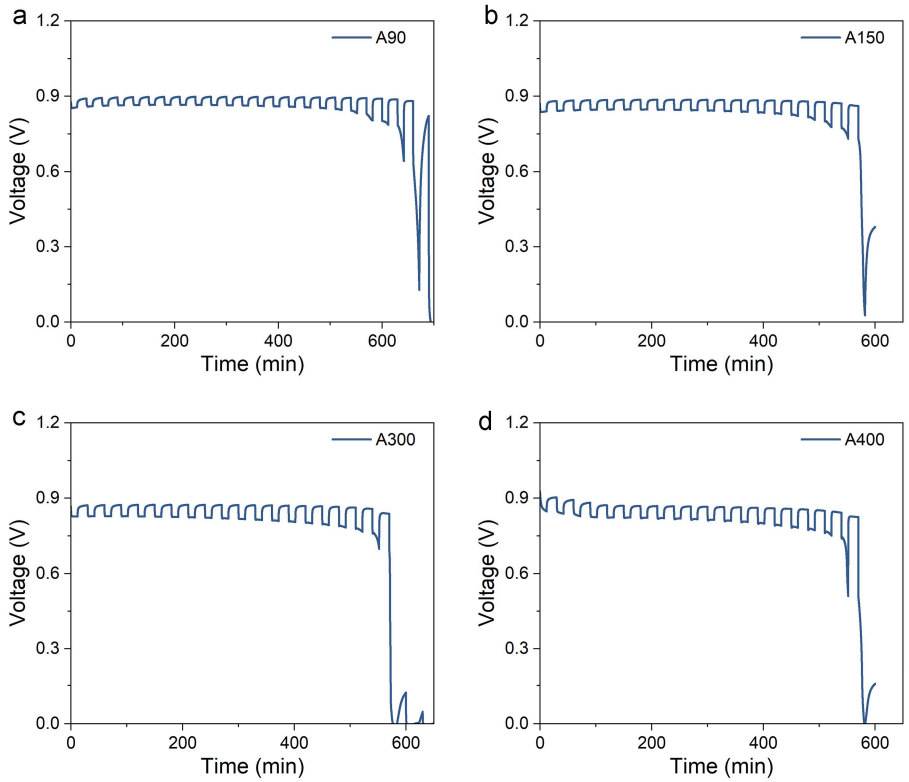
Supplementary Fig. 22 Proton adsorption in DRT. DRT curves of (a) A90 and (d) A400 at selected τ range during discharge. The τ values corresponding proton adsorption on lattice oxygen in A90, A150, A300 and A400 at different states of discharge. The peak associated with lattice oxygen adsorption protons in A90 shifts leftward until vanishing with discharge depth, suggesting rapid proton adsorption. A400 exhibits a distinct proton adsorption peak over the entire discharge period. The τ for proton adsorption on lattice oxygen increases with O_{pl} concentration.



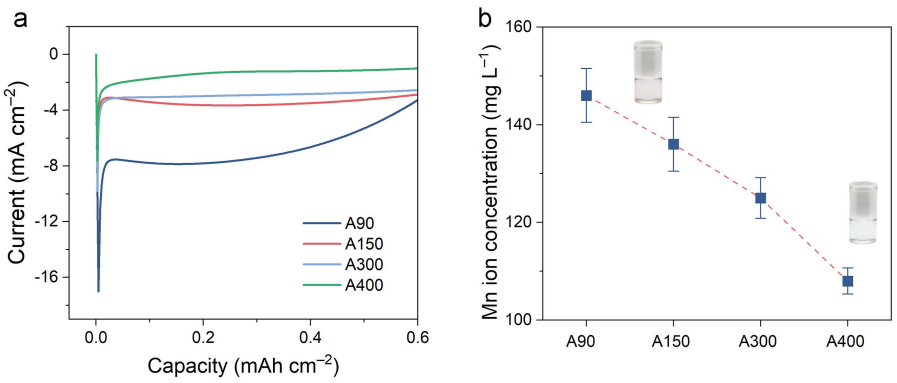
Supplementary Fig. 23 The structure of MnO_2 with tunnel. The structure models of γ-MnO_2 with 1 × 2 tunnels and β-MnO_2 with 1 × 1 tunnels. Proton adsorption on O_{py} sites of γ-MnO_2 sites is accelerated due to the broadened tunnelling pathways in the γ-MnO_2 structure compared to the β-MnO_2 structure.



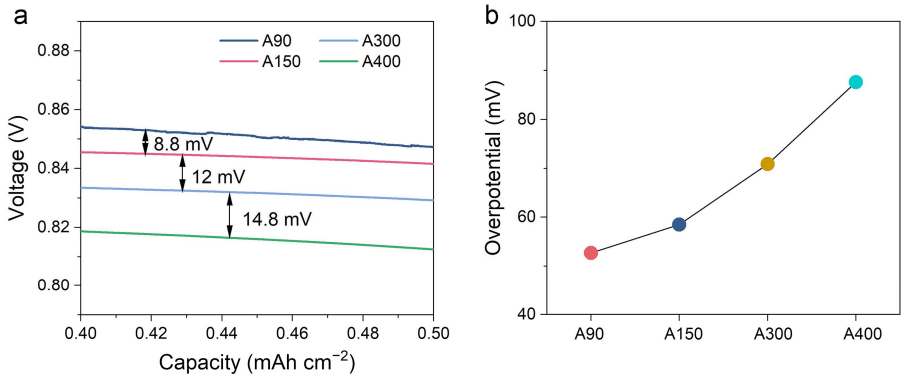
Supplementary Fig. 24 The Mn migration analysis in DRT. The τ values corresponding Mn migration in A90, A150, A300 and A400 at different states of discharge. The τ values for Mn migration decrease with O_{pl} concentration, which benefits from the facilitated lattice oxygen dissolution in O_{py} dominated A90 with rapid proton adsorption.



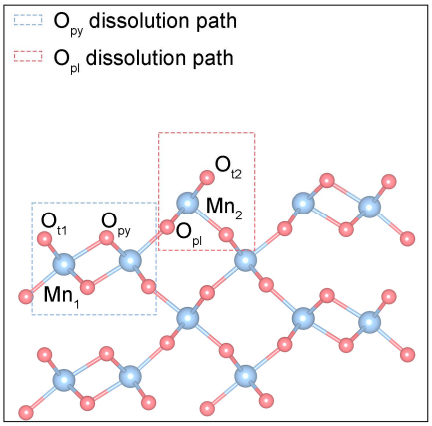
Supplementary Fig. 25 GITT data of the prepared MnO_2 samples. Voltage curve for the GITT measurements of (a) A90, (b) A150, (c) A300 and (d) A400.



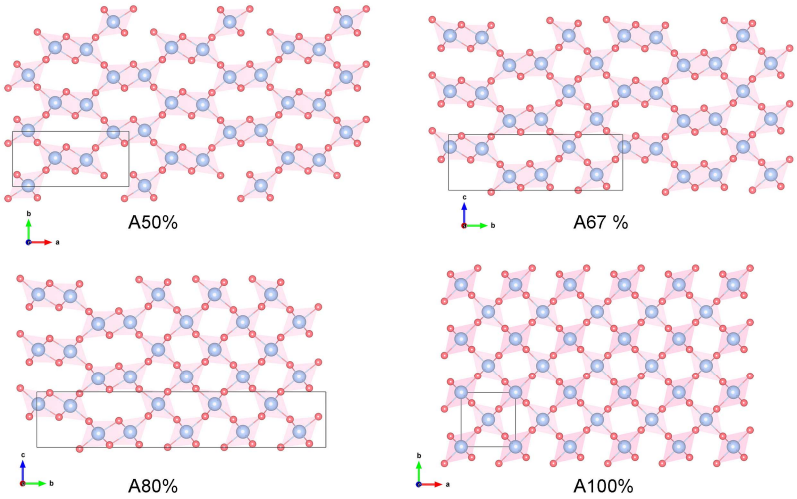
Supplementary Fig. 26 Mn dissolution ICP-AES analysis of the prepared MnO_2 samples. (a) The current curves and (b) Mn ion concentration of A90, A150, A300 and A400 upon discharge with the potentiostatic of 0.9 V (vs. Ag/AgCl) for 2 h. The insets are the optical photograph of A90 and A400 in a beaker cell containing A90 (top side) and A400 (bottom side) after discharge. The Mn ion concentration in MnO_2 dissolution for ICP-AES measurements was conducted in a beaker cell containing 0.2 m H_2SO_4 solution with MnO_2 as work electrode, AC as counter electrode and Ag/AgCl as reference electrode. In the prepared MnO_2 samples, A90 shows a high current response after applying a potentiostatic discharge, suggesting its high activity in dissolution (Supplementary Fig. 26a). However, low current response is presented in O_{pl}-dominated A400 due to its sluggish kinetics, indicating that Mn dissolution is favored on O_{py} sites compared to O_{pl} sites. ICP-AES shows that Mn ion concentration in A90 after dissolution is highest among the prepared MnO_2 samples, and it gradually decreases with increasing O_{pl} concentration.



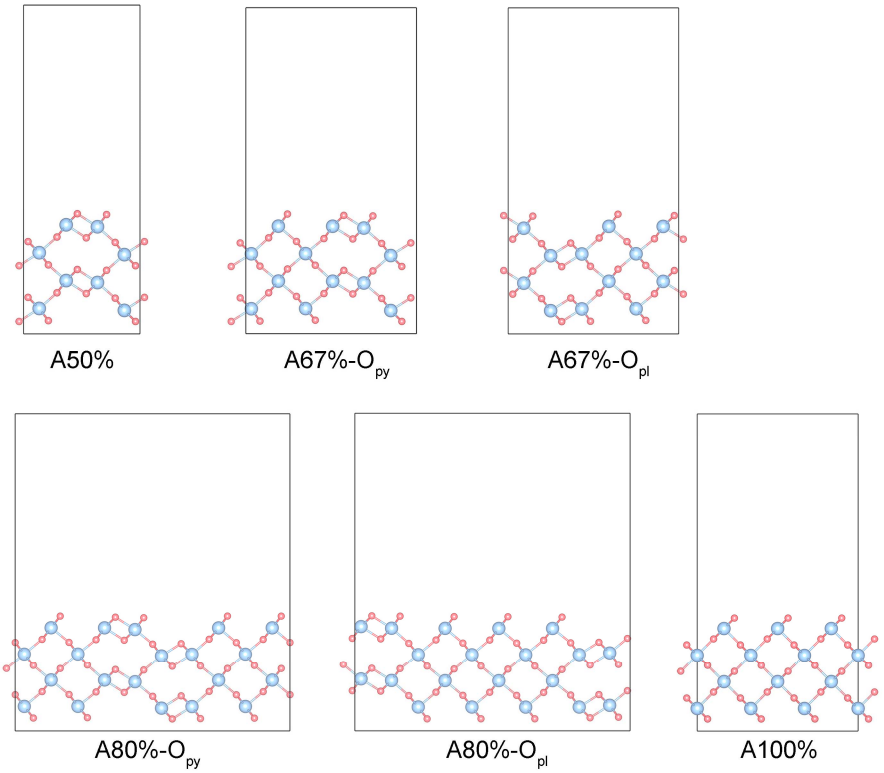
Supplementary Fig. 27 Overpotential of the prepared MnO_2 samples upon dissolution. (a) Voltage platform and (b) Overpotential of A90, A150, A300 and A400 upon discharge. The overpotential was calculated by comparing the discharge plateau voltage (defined as the discharge capacity at 0.4 mAh cm^{-2}) with the Mn-Cu cell potential (0.89 V vs Cu/Cu^{2+}).



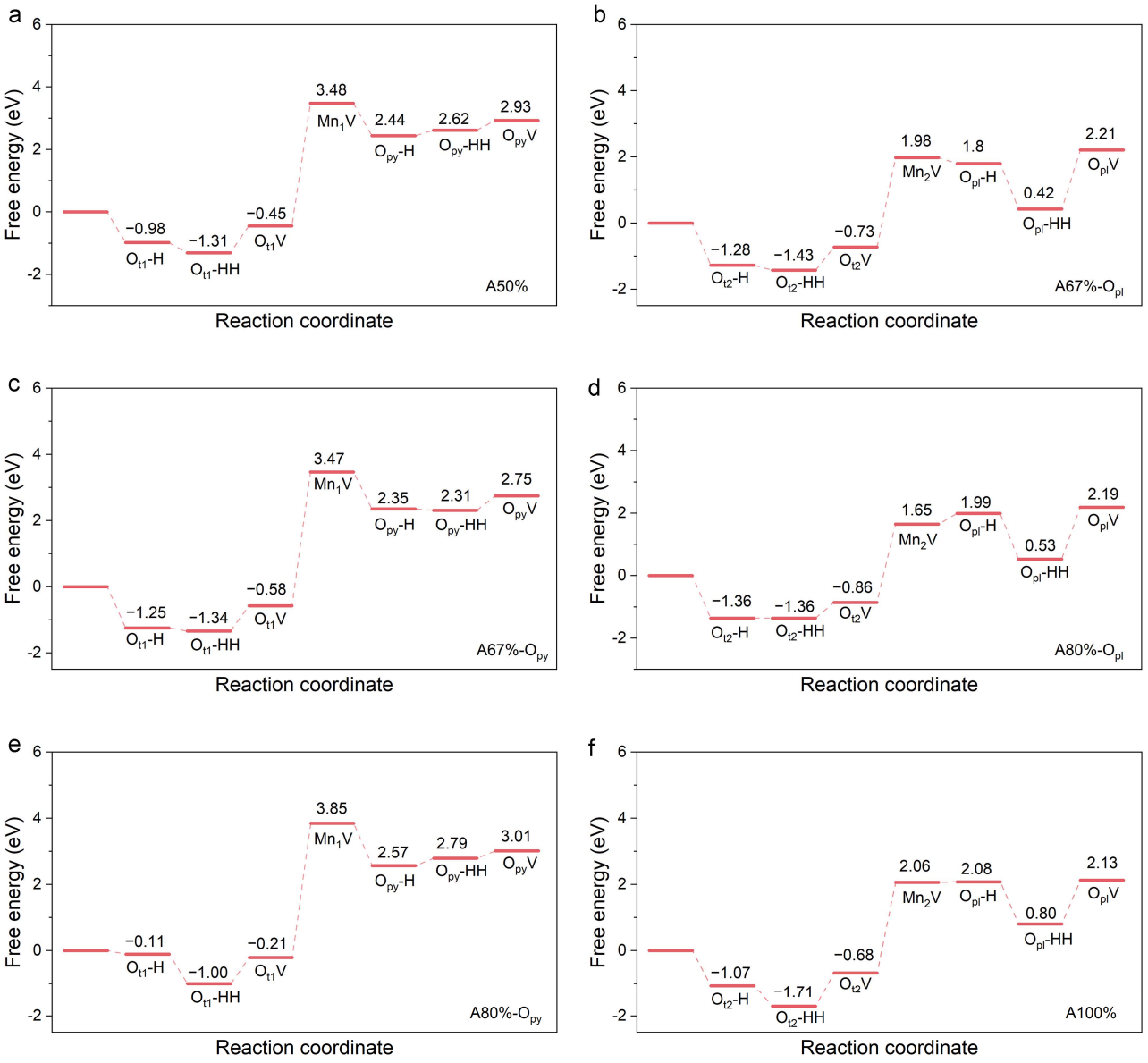
Supplementary Fig. 28 O_{py} and O_{pl} dissolution path on MnO_2. Schematic illustration of MnO_2 dissolution with O_{py} and O_{pl} involvement. The blue and red balls refer to Mn and O atoms, respectively. O_{t1} and O_{t2} represent surface oxygen. O_{py} and O_{pl} dominated mechanisms follow O_{t1}-Mn_1-O_{py} and O_{t2}-Mn_2-O_{pl}, respectively.



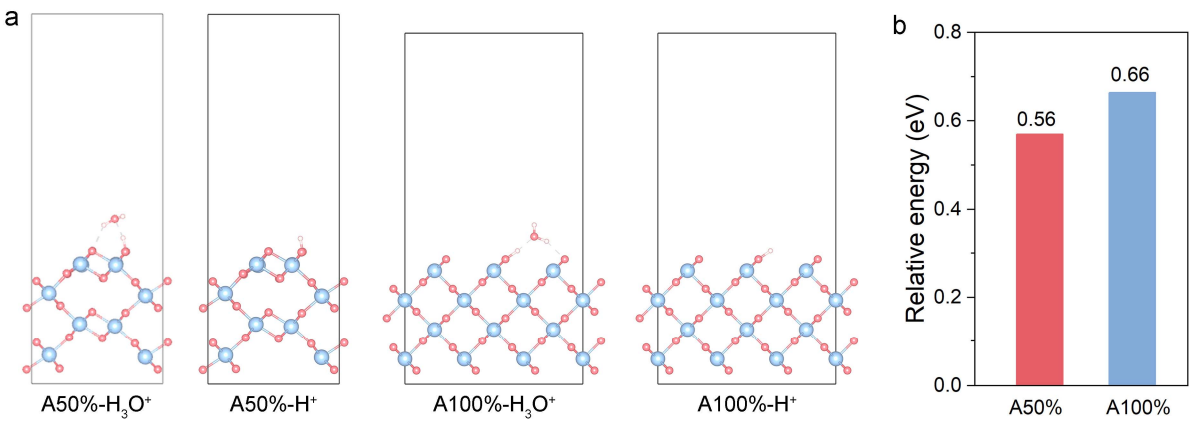
Supplementary Fig. 29 Bulk structure MnO_2 with different O_{pl} concentration. Atomic structure model of MnO_2 with the O_{pl} concentrations of 50%, 67%, 80% and 100%. Atomic models of MnO_2 with different O_{py} and O_{pl} contents were constructed based on γ-MnO_2 and β-MnO_2 symmetric references. The blue and red balls refer to Mn and O atoms, respectively. The boxes represent lattice of a unit cell.



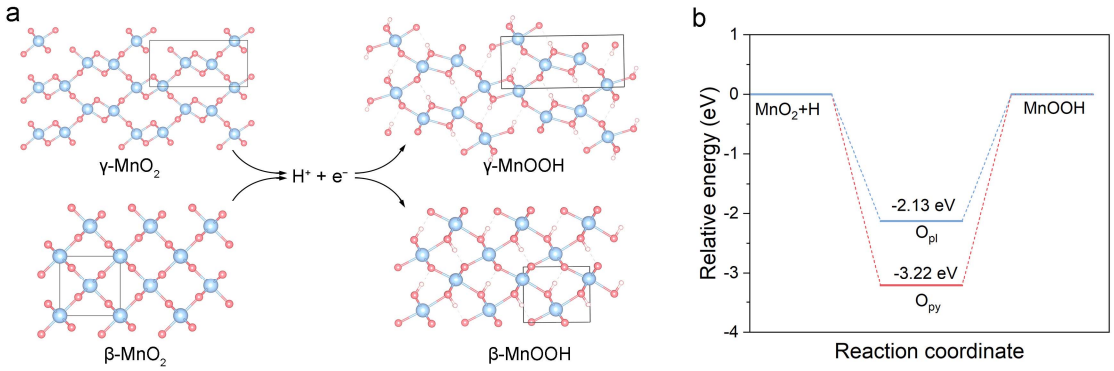
Supplementary Fig. 30 Surface structure of MnO_2 with different O_{pl} concentration. Atomic structure models of the cleaved surface for different lattice oxygen dominated MnO_2. Surface structures dominated by O_{py} and O_{pl} via symmetry were constructed on MnO_2 with O_{pl} concentration of 67%, designated as A67%-O_{py} and A67%-O_{pl} respectively. Same applies to A80%.



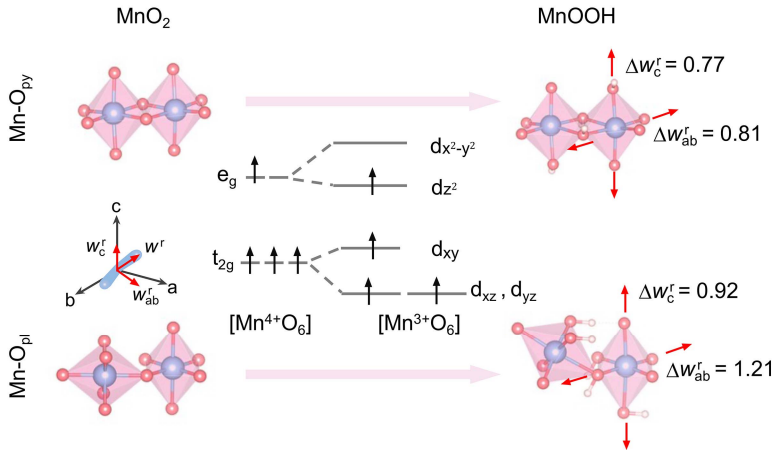
Supplementary Fig. 31 Dissolution processes of MnO_2 with different O_{pl} concentration. Free energy profiles of MnO_2 dissolution for (a) A50%, (b) A67%-O_{pl}, (c) A67%-O_{py}, (d) A80%-O_{pl}, (e) A80%-O_{py} and (f) A100% through O_{py} and O_{pl} pathway.



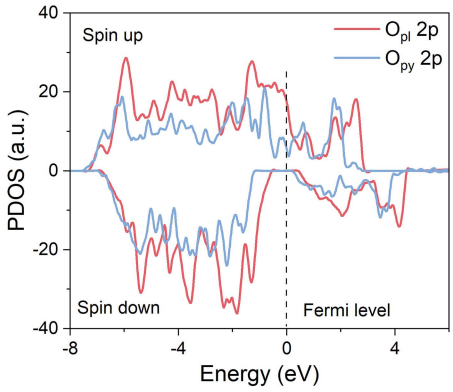
Supplementary Fig. 32 Desolvation of hydrated protons on MnO_2. (a) Atomic models of the cleaved surface for A50% and A100% adsorbed hydrated protons (H_3O^+) and protons (H^+). (b) The calculated results of desolvation energy for A50% and A100%. The desolvation energy of hydrated protons on A50% and A100% is 0.56 and 0.66, respectively. The desolvation of hydrated protons on the MnO_2 surface is the initial step in the dissolution reaction of MnO_2, which influences the dissolution of lattice oxygen and manganese.



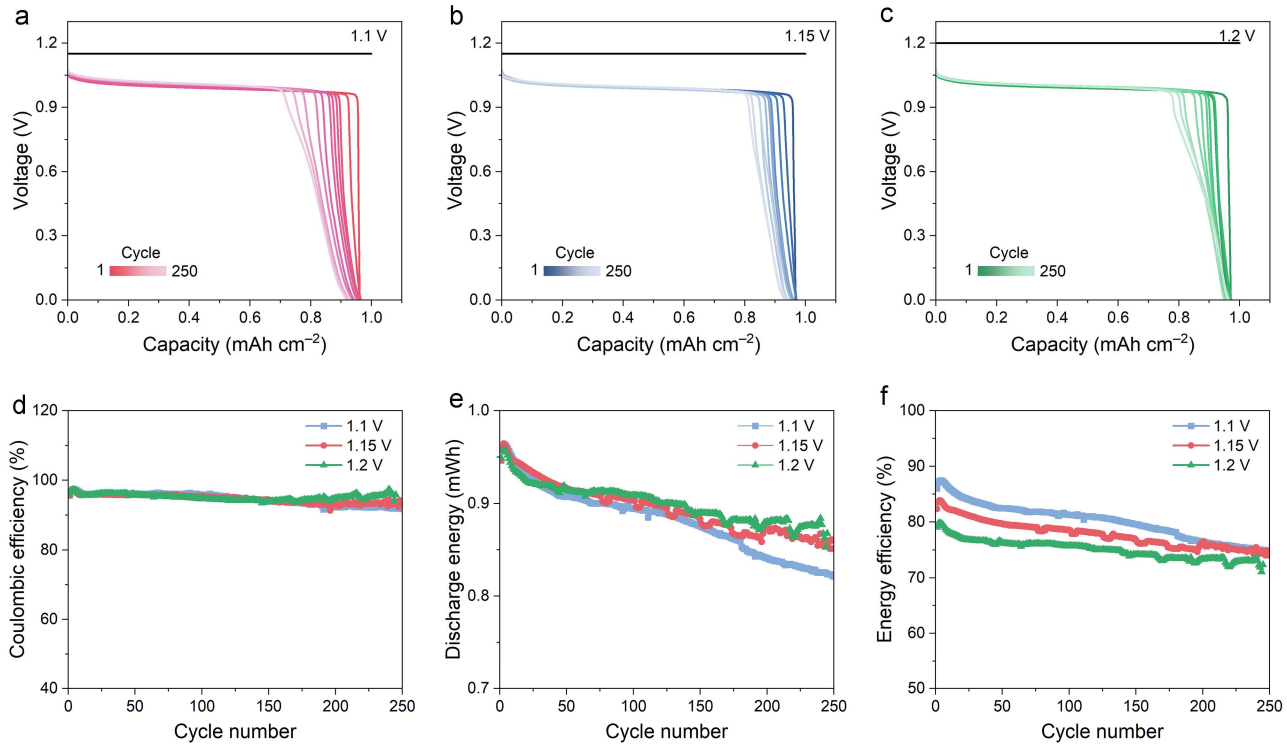
Supplementary Fig. 33 MnOOH formation free energy. (a) Atomic models of the conversion from MnO_2 to MnOOH with γ- and β-types. (b) Free energy diagrams of MnOOH formation through O_{py} and O_{pl} dominated MnO_2 with proton. The free energy of conversion reaction from O_{py} dominated γ-MnO_2 to γ-MnOOH is −3.22 eV, lower than that of reaction from O_{pl} dominated β-MnO_2 to β-MnOOH (−2.13 eV).



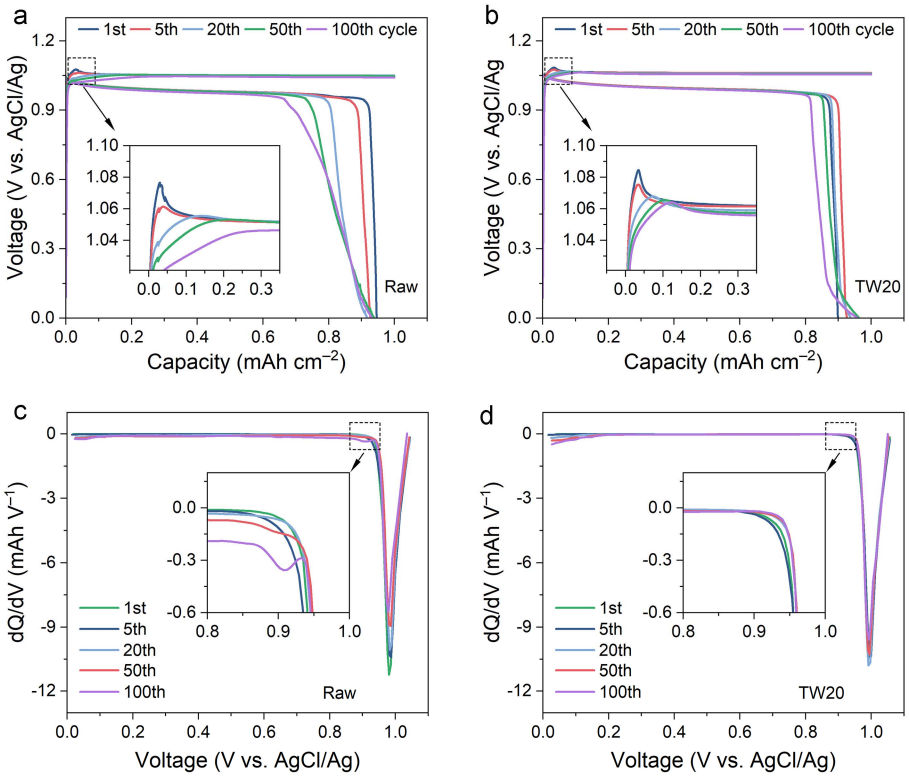
Supplementary Fig. 34 Lattice distortion during the transformation from MnO_2 to MnOOH. Schematic of Mn-O octahedra distortion in the conversion from MnO_2 to MnOOH with different lattice oxygen types. Structural distortion is unavoidable in MnOOH to eliminate degeneracy, owing to the high-spin state of Mn^{3+} with a non-symmetric 3d orbital electron configuration ($(t_{2g}\uparrow)^3(e_g\uparrow)$), which is also called the Jahn-Teller (J-T) effect[7]. The expansion and contraction of Mn-O octahedra along the ab plane ($|W_r^{ab}|$) and c-axis ($|W_r^{c}|$) directions was quantified via distortion vectors (W_r) calculated by DFT[8]. The simulated $|W_r^{ab}|$ and $|W_r^{c}|$ values in O_{py}-dominated MnOOH are 0.81 and 0.77 respectively, both lower than those in O_{py}-dominated MnOOH (1.21 for $|W_r^{ab}|$ and 0.92 for $|W_r^{c}|$). The results suggest that low structural strain in the O_{py}-dominated MnO_2 to MnOOH process promotes MnOOH formation during MnO_2 dissolution, whereas O_{pl}-dominated MnO_2 is unfavorable for MnOOH generation due to severe lattice distortion.



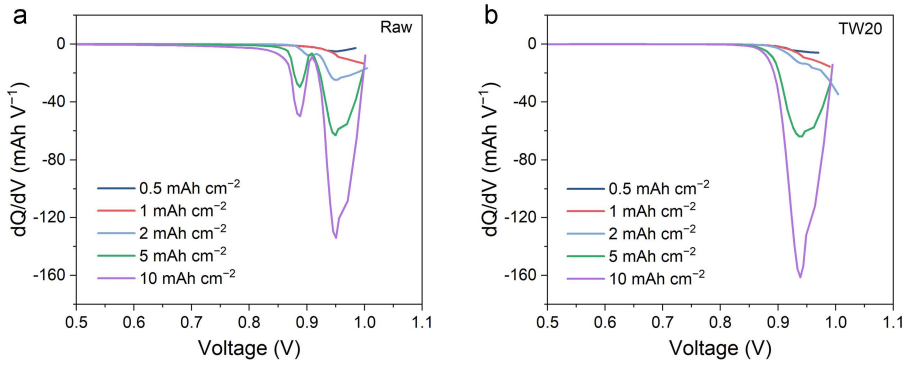
Supplementary Fig. 35 The density of states of MnO_2 with different lattice oxygen. Projected density of states profiles of spin-resolved O 2p for O_{py} and O_{pl} dominated MnO_2. The dotted line represents the Fermi level ($E_f = 0$). O_{pl} exhibits a higher density of O 2p states near the Fermi level compared with O_{py}, indicating enhanced electronic activity. There is no electron transfer during the transition from Mn*OOH to MnOOH, while the dissolution of Mn^{2+} ions from Mn*OOH requires favorable electron conduction. Consequently, the delocalized O 2p distribution in O_{py}-dominated MnO_2 will promote the conversion reaction from Mn*OOH to MnOOH.



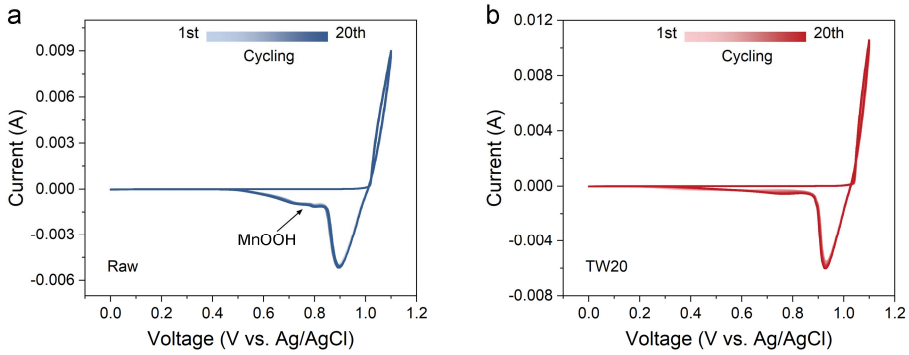
Supplementary Fig. 36 The electrochemical performance of Mn-Cu cells under different charging conditions. Voltage curves of Mn-Cu cells using raw electrolyte (0.7 m $MnSO_4$ and 0.7 m $CuSO_4$ with 0.5 m H_2SO_4) under the potentiostatic charging of (a) 1.1, (b) 1.15 and (c) 1.2 V after different cycles. (d) CE, (e) discharge energy and (f) EE of Mn-Cu cells after applied different potentiostatic charging. The galvanostatic discharge current was set to 1 mA cm^{-2}.



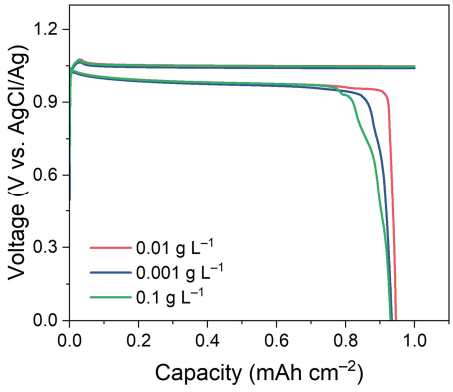
Supplementary Fig. 37 Cycle performance of MnO_2 deposition/dissolution with TW20 electrolyte. (a, b) Voltage curves and (c, d) differential capacitance (dQ/dV) profiles MnO_2 deposition/dissolution in a three-electrode beaker cell using (a, c) raw and (b, d) TW20 electrolytes under galvanostatic charge and discharge of 1 mA cm^{-2} for 1 mAh cm^{-2} at different cycles. The insets in Supplementary Figs. 37a and 37b show localized enlargements to illustrate MnO_2 nucleation during the initial stage. The voltage difference between voltage maximum and the plateau voltage in the charging curve represents the nucleation overpotential of MnO_2[9]. The MnO_2 deposition in raw electrolyte after repeated cycling exhibits no nucleation overpotential, which can be explained by residual dead manganese acting as active sites for MnO_2 nucleation due to incomplete dissolution. In contrast, upon incorporation of TW20, MnO_2 shows high dissolution reversibility with stable MnO_2 nucleation curves. The insets in Supplementary Figs. 37c and 37d reflect the generation of MnOOH intermediates during MnO_2 dissolution via an extra peak at 0.9 V. No additional peak is observed in the MnO_2 reaction using the TW20 electrolyte, indicating high reversibility with TW20 addition.



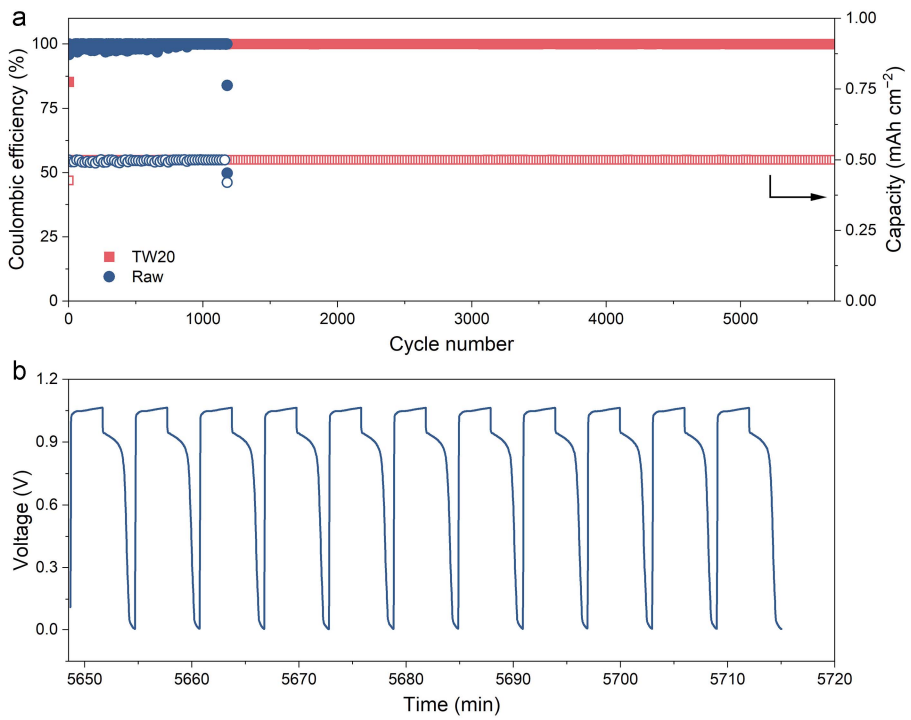
Supplementary Fig. 38 dQ/dV curves of MnO_2 dissolution with different electrolytes. dQ/dV curves of MnO_2 dissolution in Mn-Cu cells using (a) raw and (b) TW20 electrolytes at different capacities. dQ/dV curves of MnO_2 dissolution in raw electrolyte show an additional peak at 0.9 V, presumably corresponding to MnOOH formation. There is no extra peak in the TW20 electrolyte, indicating reversible MnO_2 deposition/dissolution in TW20 electrolyte.



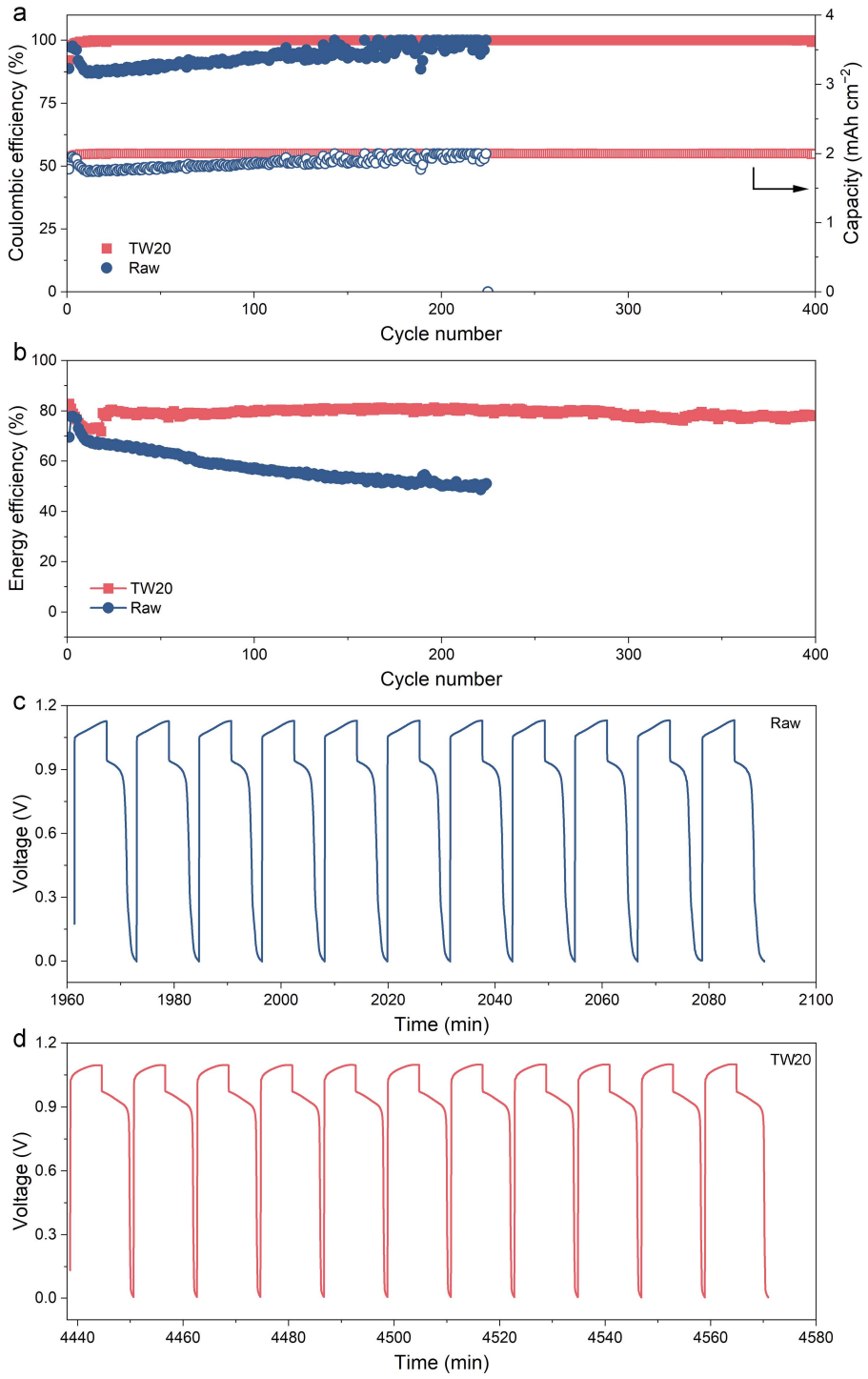
Supplementary Fig. 39 CV curves of MnO_2 deposition/dissolution with different electrolytes. (a) Raw and (b) TW20 electrolytes at a scan rate of 0.2 mV s^{-1}.



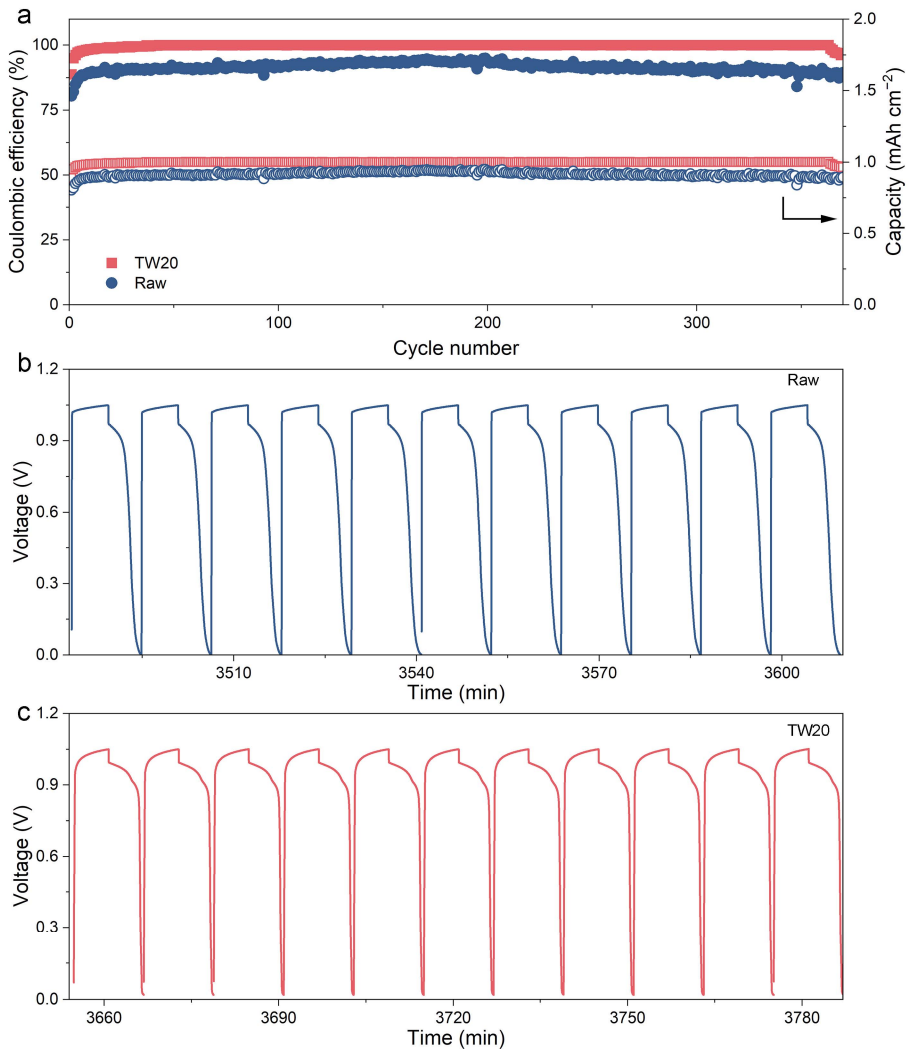
Supplementary Fig. 40 MnO_2 deposition/dissolution in different TW20 concentrations. Voltage curves of MnO_2 deposition/dissolution in a three-electrode beaker cell with three concentrations of TW20 at 1 mA cm^{-2} and 1 mAh cm^{-2}. The discharge capacity and energy of MnO_2 using a TW20 electrolyte (0.01 g L^{-1}) exceed those with the other two electrolyte concentrations.



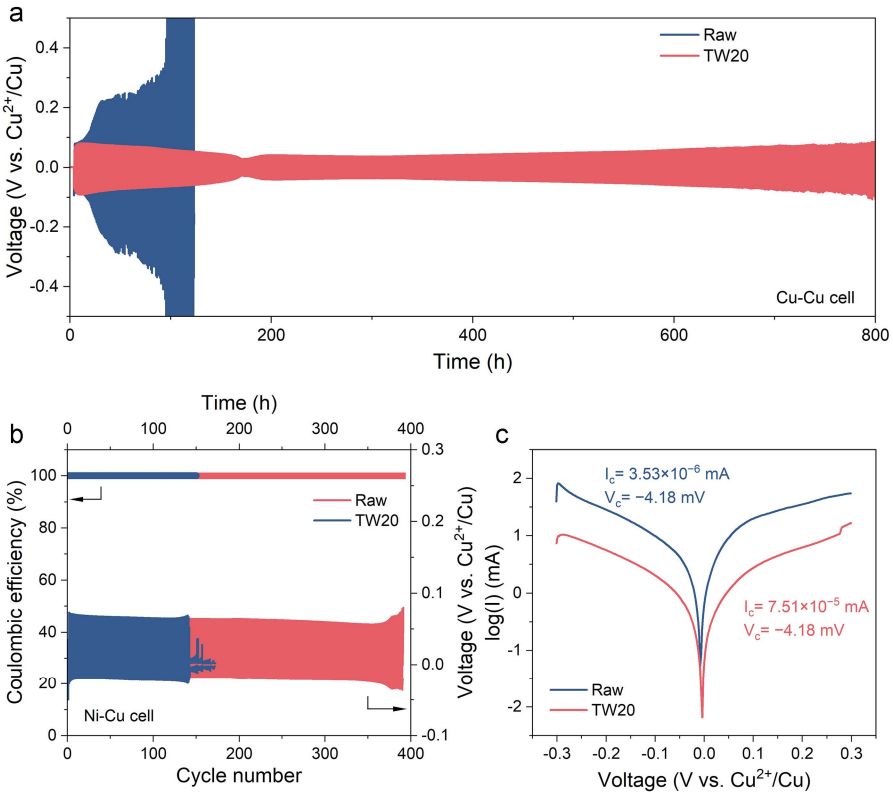
Supplementary Fig. 41 Cycle performance of Mn-Cu cells with TW20 electrolyte. (a) Cycle stability of Mn-Cu cells with raw and TW20 electrolyte at **10 mA cm^{-2} for 0.5 mAh cm^{-2}**. (b) Voltage curves of Mn-Cu cells with raw electrolyte at selected cycles.



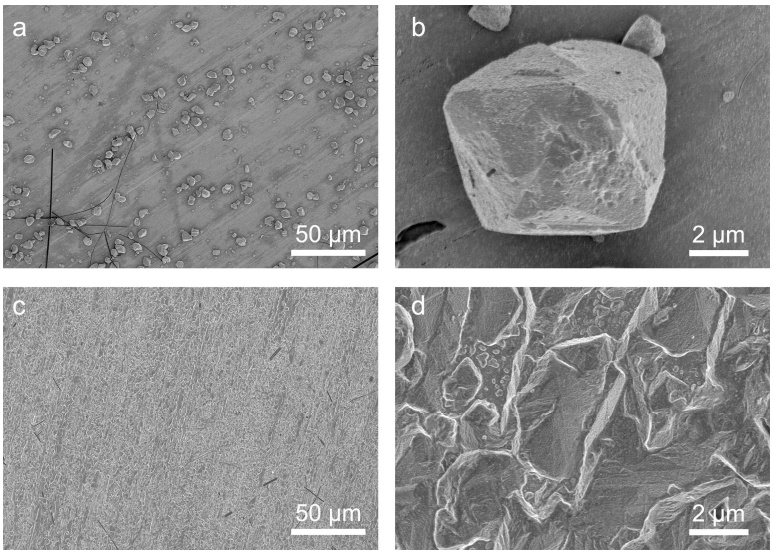
Supplementary Fig. 42 Cycle performance of Mn-Cu cells with TW20 electrolyte. (a) Cycle stability and (b) EE of Mn-Cu cells with raw and TW20 electrolyte at **20 mA cm^{-2} for 2 mAh cm^{-2}**. Voltage curves of Mn-Cu cells with (c) raw and (d) TW20 electrolytes at selected cycles.



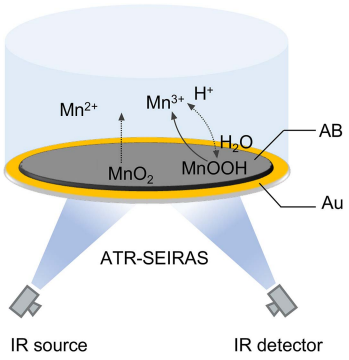
Supplementary Fig. 43 Cycle performance of Mn-Cu DEF cells with TW20 electrolyte. (a) Cycle stability of Mn-Cu DEF cells with raw and TW20 electrolyte at **10 mA cm^{-2} for 1 mAh cm^{-2}**. Voltage curves of Mn-Cu DEF cells with raw and TW20 electrolytes at selected cycles.



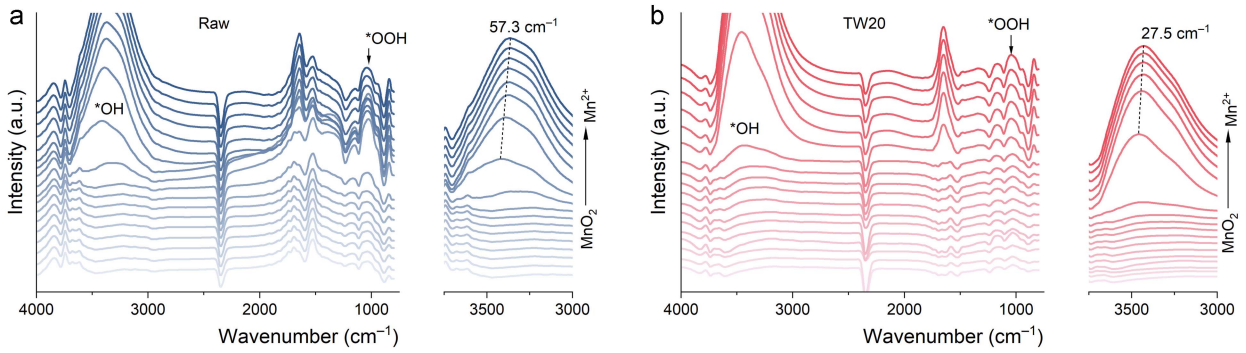
Supplementary Fig. 44 The electrochemical performance of Cu anode with TW20 electrolyte. (a) Cycle stability of Cu-Cu symmetric cells using raw (1 m $CuSO_4$ with 0.5 m H_2SO_4) and TW20 (1 m $CuSO_4$ and 0.5 m H_2SO_4 with 0.01 g L^{-1} TW20) electrolytes at a current density of 2 mA cm^{-2} for 1 mAh cm^{-2}. (b) CE and voltage curves of Ni-Cu half cells using raw and TW20 electrolytes at a current density of 1 mA cm^{-2} for 0.5 mAh cm^{-2}. (c) Tafel plots of Cu-Cu symmetric cells using raw and TW20 electrolytes. Cu-Cu symmetric cell with TW20 electrolyte can normally operate for 800 h, while the voltage of Cu-Cu symmetric cell using raw electrolyte increases after cycling for 20 h and exceeds 400 mV upon cycling for 100 h. Ni-Cu half cell using raw electrolyte fails after 100 cycles but the life span of the half cell is extended to 390 cycle upon the introduction of TW20. The Tafel curves reveal that the Cu electrode using TW20 electrolyte exhibits a lower corrosion current and a more positive potential compared to that using raw electrolyte.



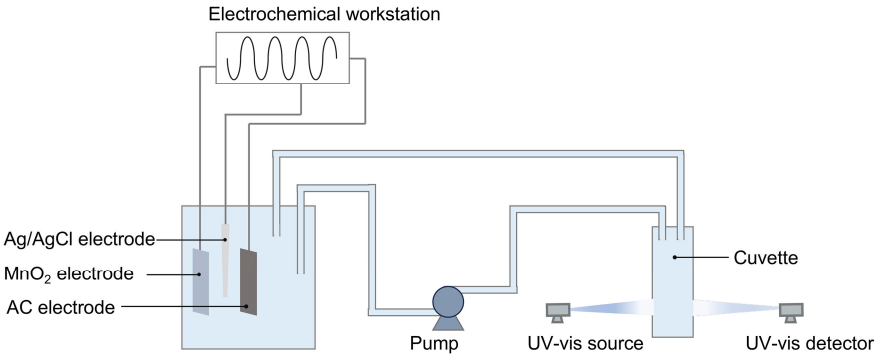
Supplementary Fig. 45 The morphology of Cu deposition with TW20 electrolyte. SEM images of Cu deposition on commercial Cu foil using (a, b) raw and (c, d) electrolytes at 1 mA cm^{-2} for 1 mAh cm^{-2}. Cu deposition in raw electrolyte shows a rough surface due to inhomogeneous Cu foil surface. However, a flat and dense surface is presented on Cu foil with TW20 electrolytes after Cu deposition.



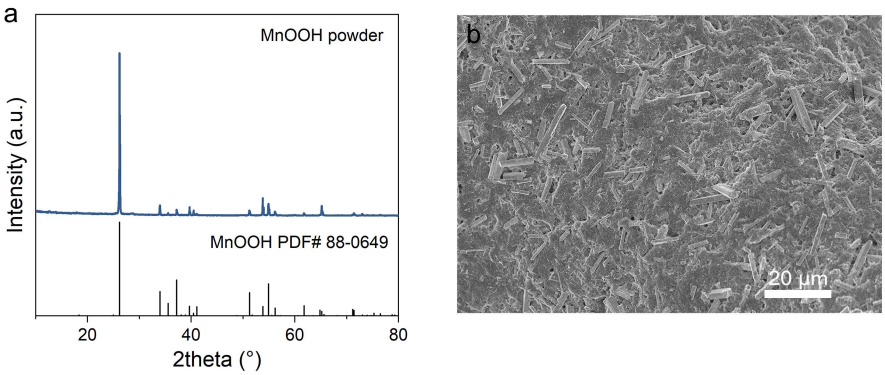
Supplementary Fig. 46 In situ infrared spectroscopy analysis. Schematic illustration of MnO_2 dissolution with intermediate products for the in situ ATR-SEIRAS measurements.



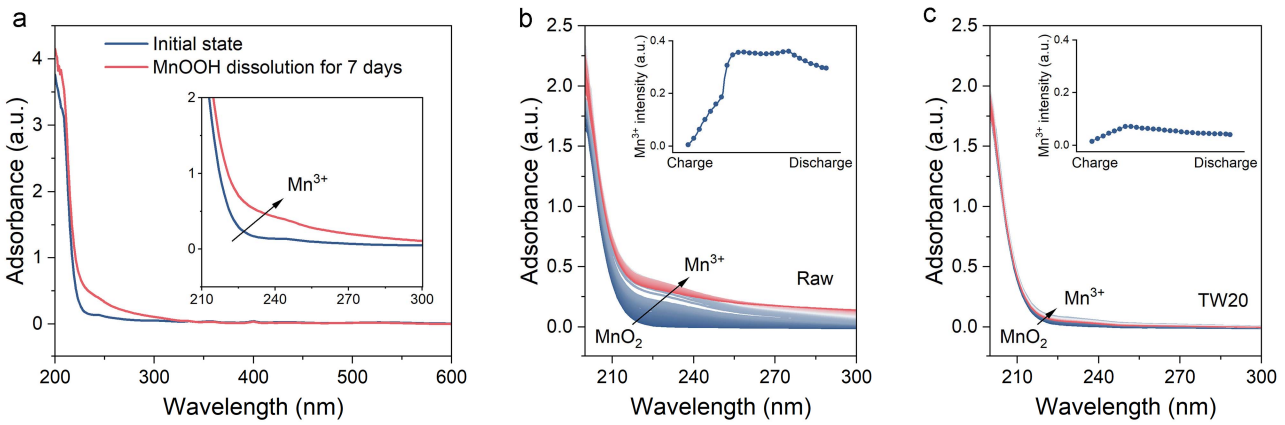
Supplementary Fig. 47 MnOOH intermediate tracking via in situ infrared spectroscopy. In situ FTIR profiles of MnO_2 dissolution within (a) raw and (b) TW20 electrolytes.



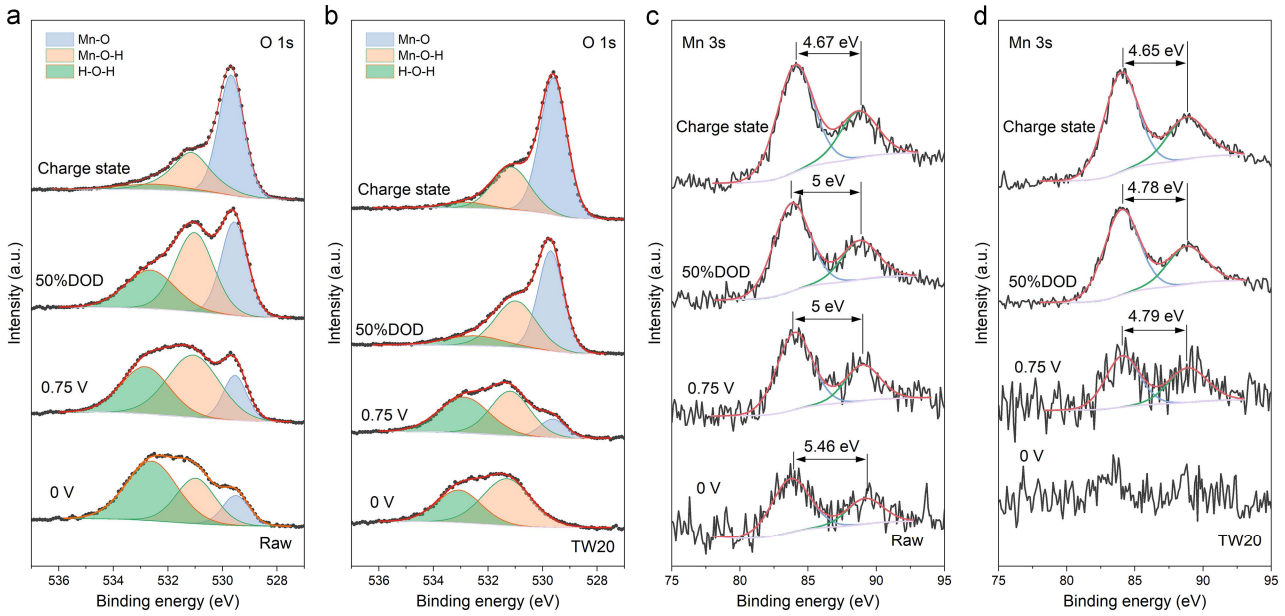
Supplementary Fig. 48 In situ UV-vis absorption spectroscopy setup. Schematic of the in situ UV-vis absorption spectroscopy measurements for the analysis of MnO_2 dissolution with intermediate products.



Supplementary Fig. 49 Structure and morphology of the prepared MnOOH. (a) XRD patterns and (b) SEM images of the prepared MnOOH powder. The crystal structure pf the synthesized MnOOH powder is indexed as MnOOH phase (PDF #88-0649). A nanorod morphology is observed in SEM images of the MnOOH powder.

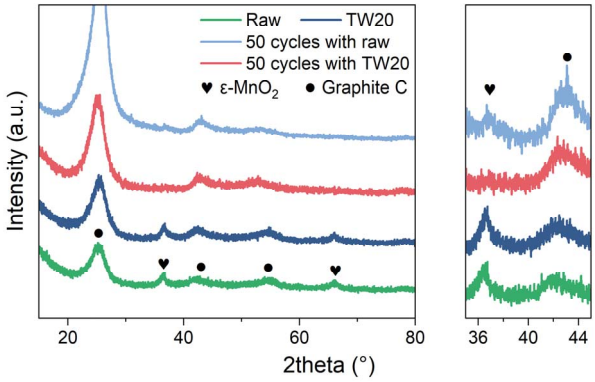


Supplementary Fig. 50 In situ UV-vis spectra of MnO_2 dissolution with and without TW20 electrolytes. (a) UV-vis spectra of MnOOH soaking in 1 m $MnSO_4$ and 0.2 H_2SO_4 solution at initial state and after 7 days. In situ UV-vis spectra of MnO_2 dissolution in (b) raw and (c) TW20 electrolytes. The inserts show Mn^{3+} concentration during discharge. To avoid baseline differences, the cuvette containing MnOOH dispersed in solution is maintained within the spectrophotometer throughout the measurements of MnOOH dissolution. The Mn^{3+} content is defined as the absorbance value at 240 nm in the UV-vis spectrum.

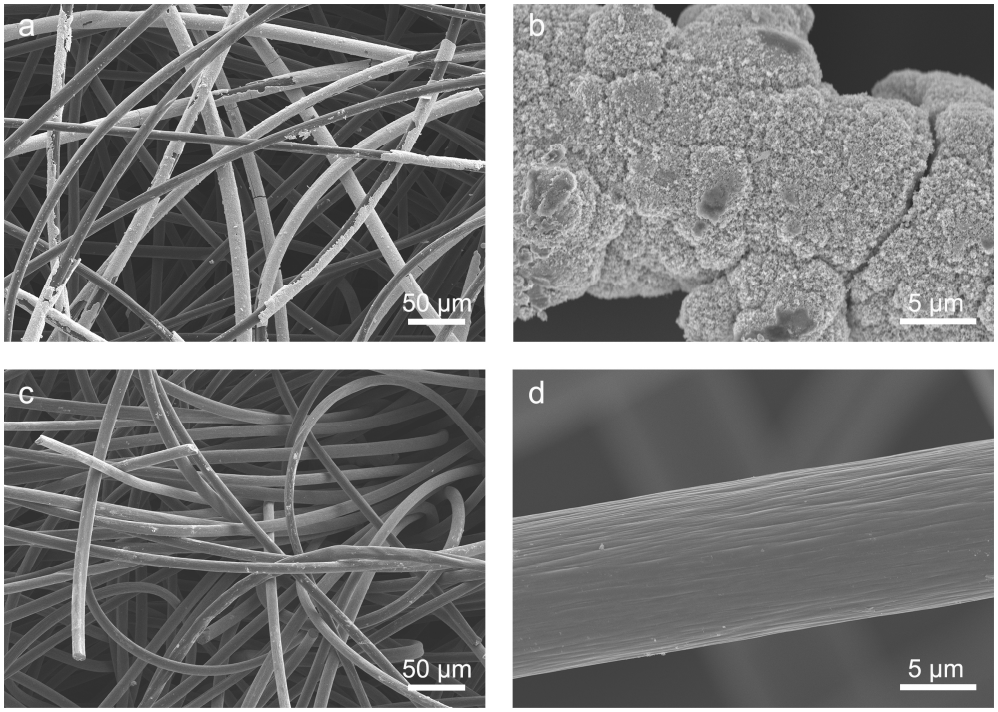


Supplementary Fig. 51 XPS analysis of post-cycled MnO_2 in different electrolytes. XPS spectra (a, b) O 1s and (c, d) Mn 3s in MnO_2 with (a, c) raw and (b, d) TW20 electrolytes after 50 cycles at charge and discharge to depth of discharge of 50%, 0.75 V and 0 V. Mn-O peaks are observed in the O 1s spectra of MnO_2 using raw electrolyte after 50 cycles discharged to 0 V, indicating the accumulation of dead manganese. However, the O 1s spectra of MnO_2 under the same operating conditions show no Mn-O signal. From the Mn 3s XPS spectra, the spin energy splitting (ΔE) of MnO_2 with raw electrolyte increased with state of discharge. The average oxidation states (AOS) of Mn are calculated from AOS = 8.956 − 1.126ΔE. In the raw electrolyte, the Mn AOS during discharge and

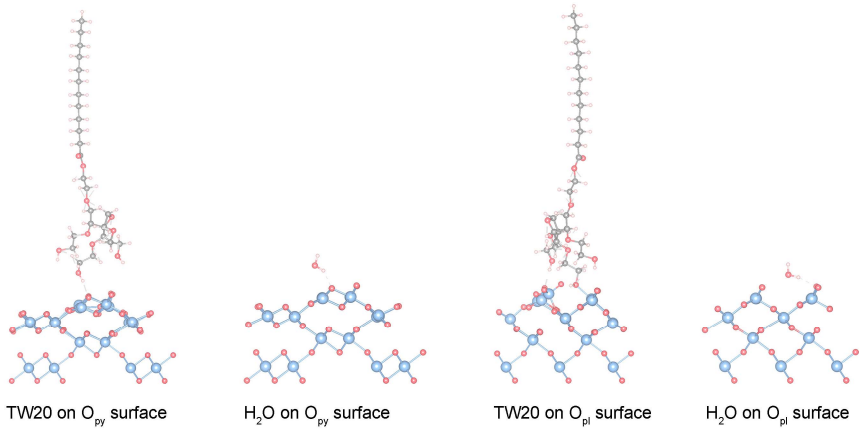
after full discharge is determined as 3.33 and 2.80, respectively, indicative of the formation of MnOOH. However, the Mn AOS during discharge with the TW20 electrolyte is approximately 3.57, suggesting a higher Mn oxidation state due to suppressed MnOOH formation.



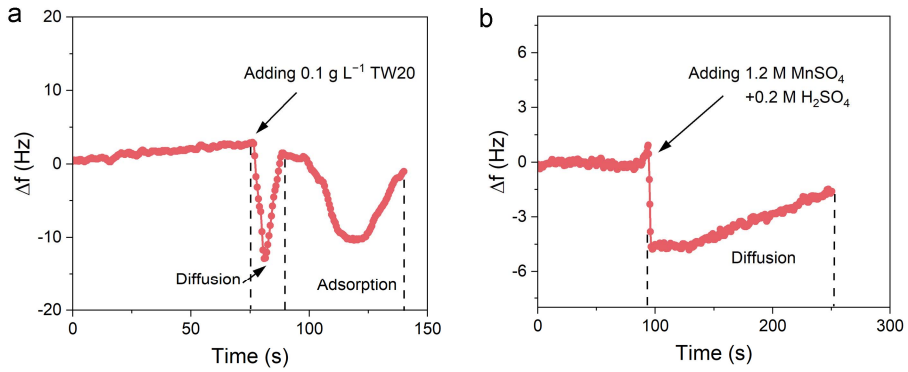
Supplementary Fig. 52 XRD analysis of post-cycled MnO_2 in different electrolytes. XRD patterns of MnO_2 with raw and TW20 electrolytes at first deposition state and after 50 cycles. The characteristic peaks associated with ε-MnO_2 are retained in the XRD pattern of MnO_2 using raw electrolyte after 50 cycles, whereas no MnO_2 signal is observed in the XRD with the TW20 electrolyte.



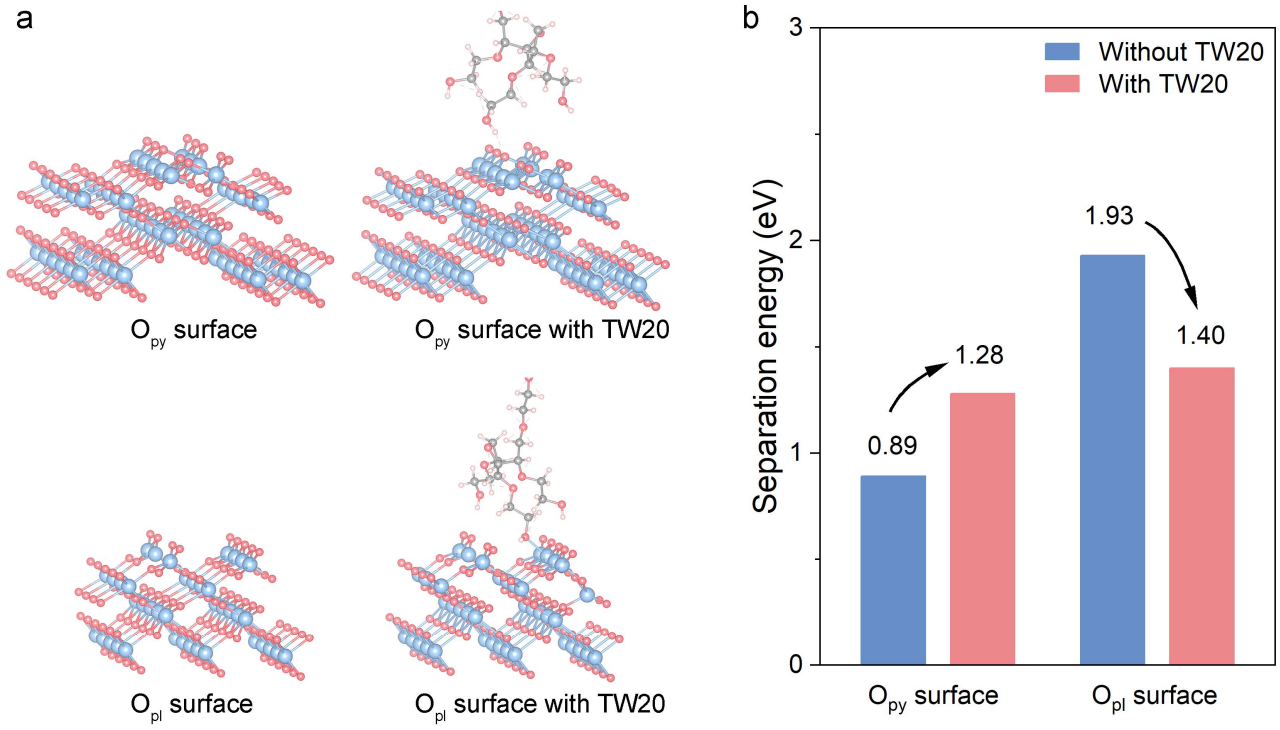
Supplementary Fig. 53 SEM analysis of post-cycled MnO_2 in different electrolytes. SEM images of MnO_2 with (a, b) raw and (c, d) TW20 electrolytes after 50 cycles. Large quantities of dead manganese are accumulated on the carbon felt electrode in the raw electrolyte after 50 cycles due to the Mn^{3+} disproportionation reaction. However, the carbon felt with the TW20 electrolyte are clean without any solid products.



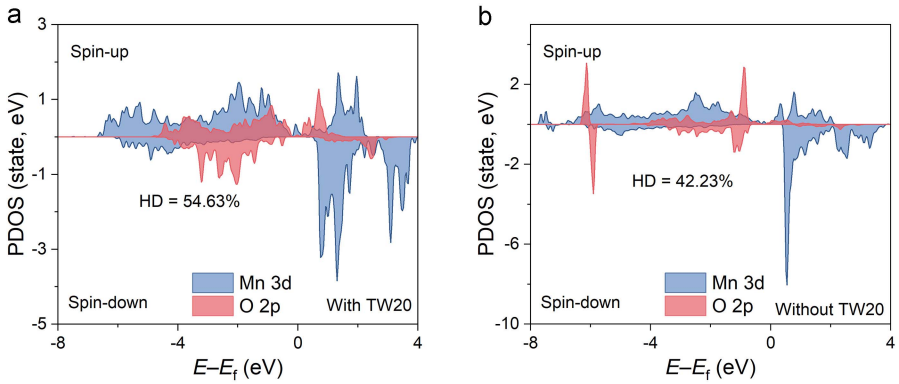
Supplementary Fig. 54 Binding energy analysis of TW20 and H_2O molecules adsorbed on ε-MnO_2. Atomic structure of TW20 and H_2O molecules adsorbed on O_{py} and O_{pl} surface of ε-MnO_2.



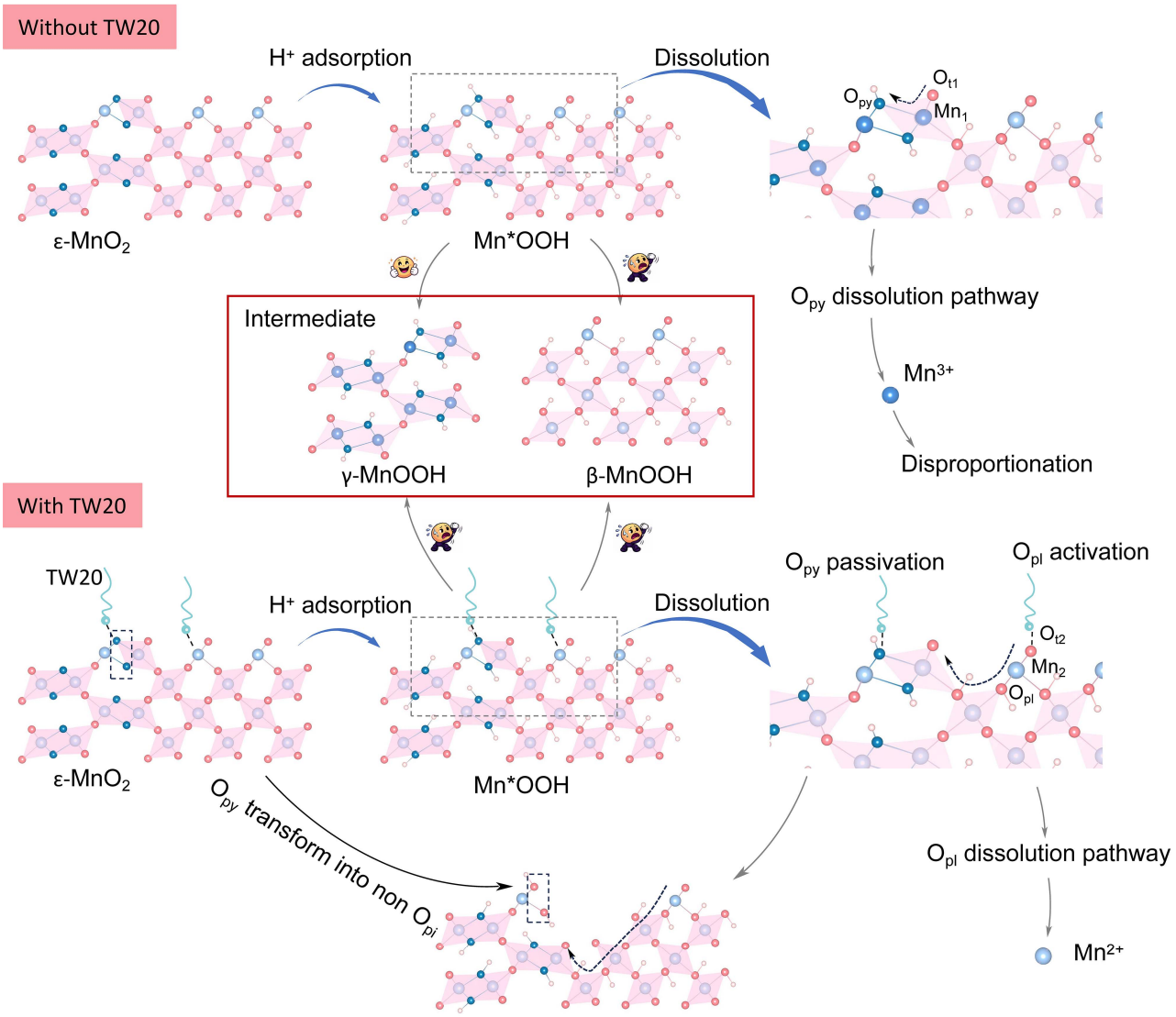
Supplementary Fig. 55 QCM analysis of interaction between TW20 and ε-MnO_2. QCM frequency response of ε-MnO_2-loaded Au electrode after the addition of (a) 0.1 g L^{-1} TW20 and (b) 1.2 m $MnSO_4$ and 0.2 m H_2SO_4 (denoted as MS) into the 1 m $MnSO_4$ and 0.2 m H_2SO_4 solution. As shown in Supplementary Fig. 55, the frequency response for the two electrolytes differs significantly. Two frequency drops are observed in TW20 while only a single frequency decline is observed in the electrolyte with the MS addition. The first sharp frequency drop is attributed to a concentration-gradient-driven response associated with solute diffusion near the Au electrode loaded with ε-MnO_2. According to Equation 1, a decrease in frequency corresponds to an increase in the effective mass of the electrode. Upon TW20 addition, the second frequency drop suggests a strong adsorption of TW20 molecules onto the MnO_2 surface[10].



Supplementary Fig. 56 Dissolution analysis of lattice oxygen on ε-MnO_2 with TW20. (a) Atomic structure of O_{py} surface (top panel) and O_{pl} surface (bottom panel) after lattice oxygen separation with TW20. (b) Separation energy of lattice oxygen from O_{py} surface and O_{pl} surface with and without TW20.



Supplementary Fig. 57 Mn-O hybridization of O_{py} surface with and without TW20. PDOS diagrams of Mn 3d and O 2p orbitals from surface oxygen of O_{py} surface (a) with and (b) without TW20.



Supplementary Fig. 58 More detail of different MnO_2 dissolution paths in ε-MnO_2. It illustrates the preferential O_{py} dissolution path in ε-MnO_2 without TW20 and O_{pl}-dominated dissolution in the presence of TW20.

Supplementary Note 1 Lattice oxygen dominated MnO_2 dissolution

The electrochemical reduction processes of MnO_2 during dissolution are given by the following equation[11].

$$MnO_2 + H^+ + e^- \rightarrow Mn^*OOH \quad (5)$$

$$Mn^*OOH \rightarrow MnOOH \quad (6)$$

$$Mn^*OOH + 3H^+ + e^- \rightarrow Mn^{2+} + 2H_2O \quad (7)$$

$$MnOOH + 3H^+ + e^- \rightarrow Mn^{2+} + 2H_2O \quad (8)$$

$$MnO_2 + 4H^+ + 2e^- \rightarrow Mn^{2+} + 2H_2O \quad (9)$$

The formed MnOOH is further chemically dissolved to produce Mn^{3+} or oxidized to MnO_2[12].

$$MnOOH + 3H^+ \rightarrow Mn^{3+} + 2H_2O \quad (10)$$

$$MnOOH \rightarrow MnO_2 + H^+ + e^- \text{ (at weak acid)} \quad (11)$$

The Mn^{3+} ions generated by the chemical reactions can electrochemical reduce to Mn^{2+} and disproportionate and hydrolyze to form inactive products[13].

$$Mn^{3+} + e^- \rightarrow Mn^{2+} \quad (12)$$

$$2Mn^{3+} + 2H_2O \rightarrow MnOOH + 3H^+ \quad (13)$$

$$2Mn^{3+} + 2H_2O \rightarrow MnO_2 + Mn^{2+} + 3H^+ \text{ (fast)} \quad (14)$$

In the O_{py} dissolution pathway, the transformation from Mn*OOH to MnOOH is accelerated by favorable proton adsorption and rapid dissolution kinetics in O_{py}-dominated MnO_2 (Equations 5 and 6). The resulting MnOOH rapidly dissolves to Mn^{3+} in acidic media (Equation 10). Free Mn^{3+} ions subsequently undergo disproportionation and hydrolysis in the aqueous electrolyte, forming MnO_2 precipitates (dead manganese) both within and outside the electrode (Equation 13). Continuous accumulation of such MnO_2 consumes active Mn^{2+} ions and protons in the electrolyte, resulting in reduced energy density and reversibility. By contrast, for the O_{pl} dissolution pathway, the MnOOH-to-MnOOH transition is thermodynamically unfavorable owing to large lattice strain. Moreover, the favorable electronic conductivity of O_{pl}-dominated MnO_2 promotes dissolution of Mn*OOH to Mn^{2+} (Equation 7), thus circumventing Mn^{3+} disproportionation and suppressing dead manganese formation.

Supplementary Note 2 MnO_2 dissolution regulated by TW20

Formation of MnOOH requires rapid proton adsorption at lattice-oxygen sites to generate MnOOH intermediates. O_{py} sites provide favorable proton adsorption positions, and their unique 1 × 2 tunnel structure offers efficient pathways for proton transport. As shown in Supplementary Fig. 58, ε-MnO_2 transforms into Mn*OOH during proton adsorption in the raw electrolyte. The O_{py}-dominated Mn-O_6 region on Mn*OOH can readily transform into the γ-MnOOH intermediate due to thermodynamic favorability and slight lattice distortion. The formation of the β-MnOOH intermediate is restricted on the O_{pl} region of Mn*OOH due to a large thermodynamic barrier. Consequently, the dissolution reaction proceeds along the O_{py}-dominated pathway, accompanied by a competing reaction involving the chemical dissolution of γ-MnOOH to generate Mn^{3+} ions, leading to a disproportionation reaction. However, in the presence of TW20, the formation of the γ-MnOOH intermediate is hindered on Mn*OOH containing O_{py}, as the Mn-O bond on the O_{py} surface is passivated by TW20. Moreover, TW20 can activate O_{pl} sites, prompting MnO_2 dissolution towards the O_{pl} pathway (O_{t2}–Mn_2–O_{pl}). In the O_{pl} dissolution pathway, one of the Mn atoms in the Mn-Mn edge is detached, thereby disrupting the original Mn-Mn edge framework. Once a Mn atom is released from the Mn-Mn_{edge} pair, O_{py} transforms into non-lattice oxygen (O_{pi}) due to the loss of the connected Mn-O_6 octahedron. Subsequent dissolution continues along the O_{pl} pathway, gradually disrupting adjacent Mn-Mn_{edge} pairs, thus inhibiting O_{py}-dominated dissolution and its competing reactions. Therefore, ε-MnO_2 dissolution is redirected toward the O_{pl} pathway through the dual regulation of O_{py} passivation and O_{pl} activation by TW20, fundamentally circumventing MnOOH intermediate formation and Mn^{3+}

disproportionation.

Supplementary Table 1 EXAFS fitting parameters at the Mn K-edge in A90, A150, A300 and A400 (S_0^2=0.66).

Samples	Path	*C.N.*	*R* (Å)	$\sigma^2\times10^3$ (Å^2)	ΔE (eV)	*R* factor
Mn foil	Mn-Mn	12*	2.49±0.009	6.52±0.54	5.69±0.63	0.006
A90	Mn-O_{pl}	4.01±0.62	1.83±0.46	0.60±1.12	7.28±1.43	0.006
	Mn-O_{py}	1.92±0.26	1.94±0.21	4.13±1.06		
	Mn-Mn_{edge}	4.71±0.81	2.86±0.02	4.84±3.45		
	Mn-Mn_{corner}	1.43±0.69	3.40±0.02	1.44±2.32		
A150	Mn-O_{pl}	4.09±0.71	1.81±0.46	1.82±3.21	8.39±1.22	0.011
	Mn-O_{py}	1.87±0.69	1.92±0.21	2.48±2.16		
	Mn-Mn_{edge}	3.77±0.55	2.84±0.02	5.66±3.58		
	Mn-Mn_{corner}	2.35±0.47	3.39±0.02	3.03±2.05		
A300	Mn-O_{pl}	4.04±0.62	1.81±0.34	0.82±2.56	7.44±2.05	0.012
	Mn-O_{py}	1.72±0.45	1.92±0.15	4.44±2.34		
	Mn-Mn_{edge}	3.97±0.36	2.85±0.03	2.70±4.15		
	Mn-Mn_{corner}	4.31±0.62	3.39±0.02	3.98±3.04		
A400	Mn-O_{pl}	4.22±0.65	1.85±0.06	0.44±2.63	6.47±0.92	0.005
	Mn-O_{py}	1.53±094	1.96±0.03	6.18±1.36		
	Mn-Mn_{edge}	1.62±0.65	2.88±0.01	2.31±2.51		
	Mn-Mn_{corner}	3.91±0.51	3.41±0.01	2.05±1.33		

Supplementary Table 2 Fitting parameters of XPS spectra of O 1s in A90, A150, A300 and A400.

Samples	Name	Peak position (eV)	FWHM (eV)	$O_{pl}/(O_{pl}+O_{py})$ ratio
A90	O_{py}	529.90	0.88	80.02%
	O_{pl}	529.50	0.88	
A150	O_{py}	529.95	0.87	69.26%
	O_{pl}	529.55	0.88	
A300	O_{py}	529.95	0.88	58.78%
	O_{pl}	529.55	0.88	
A400	O_{py}	529.95	0.92	41.95%
	O_{pl}	529.50	0.92	

Supplementary Table 3 Fitting parameters of XPS spectra of Mn 2p in A90, A150, A300 and A400.

No	Name	Peak position (eV)	A90		A150		A300		A400	
			FWHM (eV)	At%	FWHM (eV)	At%	FWHM (eV)	At%	FWHM (eV)	At%
1	Mn^{3+}	640.6	1.05	3.45	1.05	4.04	1.05	4.59	1.05	5.21
2	Mn^{3+}	641.4	1.05	3.68	1.05	4.65	1.05	4.79	1.05	4.98
3	Mn^{3+}	642.1	1.05	3.28	1.05	3.51	1.05	4.02	1.05	4.43
4	Mn^{3+}	642.8	1.05	2.61	1.05	2.51	1.05	2.85	1.05	3.23
5	Mn^{3+}	643.6	1.05	1.19	1.05	1.39	1.05	1.08	1.05	1.51
6	Mn^{3+}	644.5	1.05	0.90	1.05	1.02	1.05	0.82	1.05	1.15
7	Mn^{3+}	645.5	1.05	0.09	1.05	0.14	1.05	0.08	1.05	0.11
8	Mn^{4+}	642	1.02	40.43	1	36.72	1	36.26	1.02	34.87
9	Mn^{4+}	642.8	0.9	13.59	1	17.21	1	16.80	1	14.10
10	Mn^{4+}	643.4	0.9	12.09	0.9	9.64	1	9.85	0.9	10.03
11	Mn^{4+}	644.1	0.9	7.87	0.9	8.00	0.9	7.47	0.9	7.99
12	Mn^{4+}	644.9	0.9	5.11	0.9	4.03	0.9	4.24	0.9	4.74
13	Mn^{4+}	645.8	0.9	2.10	0.9	2.68	0.9	2.71	0.9	2.67
14	Mn^{4+}	646.9	0.9	1.02	0.9	0.72	0.9	1.25	0.9	1.30
15	Mn^{4+}	647.3	1.06	0.33	1.06	0.56	1.06	0.30	1.06	0.43
16	Mn^{2+}	641.1	0.9	2.27	0.9	3.18	0.9	2.89	0.9	3.25

Supplementary Table 4 Fitting parameters of XPS spectra of Mn 2p in A90 and A400 at different states of discharge.

No	Name	Peak position (eV)	A1 in A90		B1 in A90		A2 in A400		B2 in A400	
			FWHM (eV)	At%	FWHM (eV)	At%	FWHM (eV)	At%	FWHM (eV)	At%
1	Mn^{3+}	640.3	1.05	0.45	1.05	1.90	1.05	3.94	1.05	10.58
2	Mn^{3+}	641.1	1.06	8.30	1.03	8.91	1.05	15.43	1.05	14.58
3	Mn^{3+}	641.7	1.05	10.01	1.05	10.25	1.05	8.03	1.05	16.16
4	Mn^{3+}	642.5	1.05	10.39	1.05	11.61	1.05	6.55	1.05	4.88
5	Mn^{3+}	643.3	1.05	9.49	1.05	10.00	1.05	6.11	1.05	2.47
6	Mn^{3+}	644.2	1.05	5.00	1.05	5.42	1.05	2.89	1.05	0.01
7	Mn^{3+}	645.2	1.05	2.60	1.05	3.85	1.05	2.13	1.05	0.03
8	Mn^{4+}	642.1	0.84	21.35	0.82	19.89	1.07	24.90	1.07	22.41
9	Mn^{4+}	642.85	1.05	14.95	1.05	14.90	1.05	9.71	1.05	16.62
10	Mn^{4+}	643.6	1.05	7.57	1.05	7.71	1.05	11.98	1.05	10.45
11	Mn^{4+}	644.2	1.05	5.24	1.05	2.89	1.05	2.94	1.05	0.84
12	Mn^{4+}	644.9	1.05	1.49	1.05	2.15	1.05	2.85	1.05	0.01
13	Mn^{4+}	645.8	1.05	3.16	1.05	0.52	1.05	2.54	1.05	0.96

Supplementary Table 5 Comparison of EE and stability between Mn-Cu batteries regulated by lattice oxygen topology and previously reported Mn^{2+}/MnO_2 based batteries

Mn-based batteries	Energy efficiency	Cycling number	Electrolytes	Charging protocols		Charging capacity (mAh cm^{-2})	Ref.
Mn-H	53%	1400	1 M $MnSO_4$ + 0.05 M H_2SO_4	Constant voltage (V)	1.6	1	[14]
Mn/ga-H	59%	210	1 M $MnSO_4$ + 0.1 M H_2SO_4		1.6	20	[15]
Mn-Cu	72%	2000	0.3 M $CuSO_4$ + 0.3 M $MnSO_4$ + 0.5 M H_2SO_4		1.2	0.8	[1]
Mn-Bi	65%	200	0.1 M $Bi(NO_3)_3$ + 0.1 M $MnSO_4$ +1 M HNO_3		1.2	0.8	[1]
Mn-Sn	56%	2400	2 M $MnSO_4$ + 0.3 M H_2SO_4 + 0.1 M $SnSO_4$		2.1	0.5	[16]
Mn/LC-Zn	73%	1000	1 M $ZnSO_4$ + 1 M $MnSO_4$ + 0.1 mM surfactant		2.3	0.5	[17]
Mn/PVP-Zn	82%	2000	1 M $ZnSO_4$ + 1 M $MnSO_4$ + 0.1 M H_2SO_4 + 0.07 mM PVP		2.2	4	[18]
Mn/H^+-Cu	78%	1000	0.5 M H_2SO_4 + 0.8 M $CuSO_4$ + 0.8 M $MnSO_4$		1.2	1	[19]
Mn/I_2-Zn	70%	950	1 M $MnSO_4$ + 1 M $ZnSO_4$ + 0.075 M ZnI_2		2.2	10	[20]
Mn/Eu-Zn	75%	5000	1 M $Zn(OTf)_2$ + 0.5 M $MnCl_2$ in SL + DMSO + H_2O		2.3	0.5	[21]
Mn/Mu-Zn	67%	800	2 M $ZnSO_4$ + 0.5 M $MnSO_4$ + 7 M methylurea		2.2	5	[22]
Mn/PO_4-Zn	77%	1600	1 M $ZnSO_4$ + 0.5 M $MnSO_4$ + H_3PO_4/H_2SO_4		2.2	2	[23]
Mn/SiO_2-Zn	75%	550	1 M $ZnSO_4$ + 1 M $MnSO_4$ + 0.02 M $FeSO_4$ 0.1 M H_2SO_4 + 75 mg mL^{-1} SiO_2	Constant current ($mA\ cm^{-2}$)	15	10	[24]
Mn/gel-Cu	55%	370	PAM gel soaking in 3 m $Cu(ClO_4)_2$ + 1 m $Mn(ClO_4)_2$		10	0.5	[25]
Mn-Cu	87%	5800	0.5 m H_2SO_4 + 0.7 m $CuSO_4$ + 0.7 m $MnSO_4$ + 0.01 g L^{-1} TW20		0.5	10	This work
	90%	370			1	10	

Supplementary Table 6 The calculated results of HD of O_{py} surface in ε-MnO_2 with and without TW20 by analyzing PDOS. (O_t refers to surface oxygen in O_{py} surface)

Structure	Mn-O bond	Spin-up	Spin-down	Total
O_{py} surface	Mn-O_t	60.65%	23.93%	42.23%
	Mn-O_{py}	90.07%	32.23%	60.93%
O_{py} surface with TW20	Mn-O_t	76.37%	33.20%	54.63%
	Mn-O_{py}	90.25%	41.22	65.57%

References

1. Liang, G. *et al.* A universal principle to design reversible aqueous batteries based on deposition–dissolution mechanism. *Adv. Energy Mater.* **9**, 1901838 (2019).
2. Rudolph, W. W. & Irmer, G. Raman Spectroscopic Investigation of Speciation in $MnSO_4$(aq). *J. Solution Chem.* **43**, 465–485 (2014).
3. Li, X. *et al.* Deciphering anomalous zinc ion storage in intermediate-state MnO_2 during layer-to-tunnel structural transition. *Energy Environ. Sci.* **17**, 9195–9204 (2024).
4. Pahari, S. K. & Chen, Y.-T. *In situ* spectroelectrochemical detection of oxygen evolution reaction intermediates with a carboxylated graphene–MnO_2 electrocatalyst. *ACS Appl. Mater. Interfaces* **14**, 5177–5182 (2022).
5. Wang, J. *et al.* Unlocking superior proton-storage contribution and structure stability by synergistic dual-ion modulation in *δ*-MnO_2 cathodes for aqueous zinc-ion batteries. *Mater. Today Energy* **53**, 102027 (2025).
6. Maradesa, A. *et al.* Advancing electrochemical impedance analysis through innovations in the distribution of relaxation times method. *Joule* **8**, 1958–1981 (2024).
7. Gehring, G. A. & Gehring, K. A. Co-operative Jahn-Teller effects. *Rep. Prog. Phys.* **38**, 1 (1975).
8. Wang, S. *et al.* Cooperative Jahn-Teller effect and engineered long-range strain in manganese oxide/graphene superlattice for aqueous zinc-ion batteries. *Nat. Commun.* **16**, 5191 (2025).
9. Yang, Z. *et al.* Revealing the two-dimensional surface diffusion mechanism for zinc dendrite formation on zinc anode. *Small* **18**, 2104148 (2022).
10. Li, Y. *et al.* A progressive nucleation mechanism enables stable zinc stripping–plating behavior. *Energy Environ. Sci.* **14**, 5563–5571 (2021).
11. Nijjer, S. *et al.* Oxidation of manganese(II) and reduction of manganese dioxide in sulphuric acid. *Electrochim. Acta* **46**, 395–399 (2000).
12. Lee, J. A. *et al.* The electrochemical reduction of manganese dioxide in acidic solutions: Part I.

Voltammetric peak 1. *J. Electroanal. Chem. Interfacial Electrochem.* **79**, 79–104 (1977).
13. Petitpierre, J.-Ph. *et al.* Oxydation Du $MnSO_4$ en dioxyde de manganese dans H_2SO_4 30%. *Electrochim. Acta* **35**, 281–287 (1990).
14. Chen, W. *et al.* A manganese–hydrogen battery with potential for grid-scale energy storage. *Nat Energy* **3**, 428–435 (2018).
15. Xiao, X. *et al.* Ultrahigh-loading manganese-based electrodes for aqueous batteries via polymorph tuning. *Adv. Mater.* **35**, 2211555 (2023).
16. Zhang, H. *et al.* A high-capacity Sn metal anode for aqueous acidic batteries. *Joule* **7**, 971–985 (2023).
17. Li, Y. *et al.* In situ formation of liquid crystal interphase in electrolytes with soft templating effects for aqueous dual-electrode-free batteries. *Nat. Energy* **9**, 1350–1359 (2024).
18. Chuai, M. *et al.* Theory-driven design of a cationic accelerator for high-performance electrolytic MnO_2–Zn batteries. *Adv. Mater.* **34**, 2203249 (2022).
19. Huang, J. *et al.* Low-cost and high safe manganese-based aqueous battery for grid energy storage and conversion. *Sci. Bull.* **64**, 1780–1787 (2019).
20. Zheng, X. *et al.* Development of high areal capacity electrolytic MnO_2–Zn battery via an iodine mediator. *Energy Environ Mater.* **6**, e12433 (2023).
21. Li, J. *et al.* Aqueous eutectic electrolytes suppress oxygen and hydrogen evolution for long-life Zn||MnO_2 dual-electrode-free batteries. *Nat. Energy* 1–14 (2026).
22. Deng, Y. *et al.* Nanomicellar electrolyte to control release ions and reconstruct hydrogen bonding network for ultrastable high-energy-density Zn–Mn battery. *J. Am. Chem. Soc.* **145**, 20109–20120 (2023).
23. Yang, H. *et al.* Stimulating the potential of Zn anodes to operate in low pH and harsh environments for highly sustainable Zn batteries. *Angew. Chem. Int. Ed.* **64**, e202419394 (2025).
24. Chen, H. *et al.* Achieving highly reversible Mn^{2+}/MnO_2 conversion reaction in electrolytic Zn-MnO_2 batteries via electrochemical-chemical process regulation. *Angew. Chem. Int. Ed.* **64**, e202423999 (2025).
25. Zhou, Q. *et al.* Enhancing the kinetics and reversibility of copper batteries *via* anionic chemistry. *Energy Environ. Sci.* **18**, 5347–5355 (2025).